# REPORT DOCUMENTATION PAGE

| 1. REPORT DATE (DD-MM-YYYY) | 2. REPORT TYPE | 3. DATES COVERED (From - To) |
|---|---|---|
| 31-05-2010 | Final Performance Report | 01-09-2008 to 28-02-2010 |

| 4. TITLE AND SUBTITLE | 5a. CONTRACT NUMBER |
|---|---|
| Experimental Studies of Coal and Biomass Fuel Synthesis and Flame Characterization for Aircraft Engines | |
| | 5b. GRANT NUMBER |
| | FA9550-08-1-0456 |
| | 5c. PROGRAM ELEMENT NUMBER |
| | 61102F |

| 6. AUTHOR(S) | 5d. PROJECT NUMBER |
|---|---|
| R. K. Agrawal, J. P. Gore, F. H. Ribeiro, W. N. Delgass, R. Lucht, L. Qiao, S. Naik, A. Smeltz, A. Sane, N. Singh | 2308 |
| | 5e. TASK NUMBER |
| | BX |
| | 5f. WORK UNIT NUMBER |

| 7. PERFORMING ORGANIZATION NAME(S) AND ADDRESS(ES) AND ADDRESS(ES) | 8. PERFORMING ORGANIZATION REPORT NUMBER |
|---|---|
| Purdue University<br>Energy Center<br>Mann Hall, Room 266<br>203 Martin Jischke Drive<br>West Lafayette, IN 47907-2022 | |

| 9. SPONSORING / MONITORING AGENCY NAME(S) AND ADDRESS(ES) | 10. SPONSOR/MONITOR'S ACRONYM(S) |
|---|---|
| Air Force Office of Scientific Research<br>875 North Randolph St.<br>Suite 325, Room 3112<br>Arlington, VA 22203-1768 | |
| | 11. SPONSOR/MONITOR'S REPORT |
| | AFRL-OSR-VA-TR-2013-1009 |

**12. DISTRIBUTION / AVAILABILITY STATEMENT**
Approved for public release; distribution is unlimited

**13. SUPPLEMENTARY NOTES**

**14. ABSTRACT**

A high pressure, optically accessible fast pyrolysis reactor aimed at eliminating char formation during biomass gasification was constructed and tested at atmospheric pressure with cellulose particles. A high pressure, optically accessible coal steam gasification system was assembled following stand alone system tests for the steam generator, coal feeder and electric heater subassemblies. A plug flow reactor model was developed to better understand the heat and mass transfer and chemical kinetic processes in the gasification reactions. A new counter flow burner suitable for simultaneous velocity and species concentration measurements of flames burning fuel vapor and air at various scalar dissipation rates is ready for experiments, and preliminary computations for this burner flame were completed. In summary, the work proposed on most tasks for the first year of the project is complete with the exception of catalyst selection for the hydropyrolysis (H2BiOil) and Hydro De-Oxygenation (HDO) processes. These two catalyst selection tasks are underway as a part of a follow-up year two project of the current program.

**15. SUBJECT TERMS**
Renewable fuels synthesis, Biomass fast hydropyrolysis and hydrodeoxygenation, $CO_2$ emissions control, Coal excess hydrogen hydro-gasification, Optical diagnostics, Detailed chemistry

| 16. SECURITY CLASSIFICATION OF:<br>Unclassified | | | 17. LIMITATION OF ABSTRACT | 18. NUMBER OF PAGES | 19a. NAME OF RESPONSIBLE PERSON<br>Julian Tishkoff |
|---|---|---|---|---|---|
| a. REPORT<br>Unclassified | b. ABSTRACT<br>Unclassified | c. THIS PAGE<br>Unclassified | UL | 50 | 19b. TELEPHONE NUMBER (include area code)<br>(703)696-8478 |

20130918409

# Experimental Studies of Coal and Biomass Fuel Synthesis and Flame Characterization for Aircraft Engines

AFOSR Grant Number: FA9550-08-1-0456

Final Performance Report
Report Period: September 1, 2008 to February 28, 2010

Prepared by:

**Dr. Rakesh Agrawal (PI)**
**765-494-4811**
**765-494-0805 (fax)**
**agrawalr@purdue.edu**

**Dr. Jay Gore (Co-PI)**
**765-494-1610**
**765-496-9322 (fax)**
**gore@purdue.edu**

Dr. Fabio H. Ribeiro (Participating Investigator)
Dr. W. Nicholas Delgass (Participating Investigator)
Dr. Robert P. Lucht (Participating Investigator)
Dr. Li Qiao (Participating Investigator)
Dr. Sameer Naik
Dr. Andrew Smeltz
Mr. Anup Sane
Mr. Navneet Singh

School of Chemical Engineering
School of Mechanical Engineering
School of Aeronautics and Astronautics

Purdue University
West Lafayette, IN 47907

## Table of Contents

## Executive Summary

**AFOSR Grant Number: FA9550-08-1-0456**
**Project Title:**
Experimental Studies of Coal and Biomass Fuel Synthesis and Flame Characterization for Aircraft Engines
**Project Period:** September 1, 2008 to February 28, 2010
**Report Period:** September 1, 2008 to February 28, 2010
**Date of Report:** May 31, 2010
**Contacts:**
Rakesh Agrawal Phone: 765-494-4811, E-mail: agrawalr@purdue.edu
Jay Gore, Phone: 765-494-1610, E-mail: gore@purdue.edu

### Project Objective:

The broad objective of the research team is to establish the feasibility of an innovative idea to develop a commercially and technically viable integrated coal/biomass-to-liquid jet fuel synthesis process while mitigating the $CO_2$ penalty. The objective of this project involved construction of experimental facilities and an apparatus for addressing specific scientific issues associated with the utilization of biomass and coal, in stand alone and synergistic modes, to produce appropriate aviation liquid fuels. Materials, designs, and experimental and analytical techniques previously developed for combustion and propulsion applications were introduced in an innovative manner in the new area of synthetic fuels. Optically accessible flame studies and flame structure computations were started for future establishment of combustion characteristics of coal and biomass synthesized fuels.

A high-pressure, optically-accessible, fast-pyrolysis reactor aimed at eliminating char formation during biomass gasification was constructed and tested at atmospheric pressure with cellulose particles. The assembly of the high-pressure coal steam gasification system was completed following stand alone system tests for the steam generator, coal feeder, and electric heater subassemblies. A plug-flow reactor model was developed to understand the heat and mass transfer and chemical kinetic processes in the gasification reactions better. A new counter-flow burner suitable for simultaneous velocity and species concentration measurements of flames burning fuel vapor and air at various scalar dissipation rates was designed and built. Preliminary computations for flames representing this burner have been completed. In summary, the work proposed on most tasks for the first year of the project was completed with the exception of catalyst selection for the hydropyrolysis (H2BiOil) and hydrodeoxygenation (HDO) reactors. Challenges with the design and construction of the reactors have led to postponement of the catalyst selection tasks.

AFOSR grant funds and voluntary cost share funds for the first year of the project have been fully (100%) expended.

## 1.0 Biomass Fast Hydropyrolysis

The biomass fast-hydropyrolysis part of the research team has been focused on:

(1) Flow visualization in a continuous, biomass-fed, atmospheric-pressure, glass reactor system. The objective was to understand proper biomass feed mechanisms and the importance of the axial temperature profile within the reactor tube.

(2) Construction of a micro, stainless-steel, batch reactor with an optical window to study the effect of the rate of biomass heating on char formation. In order to minimize the char formation in a continuous, lab-scale, flow reactor, it has been important to have an adequate understanding of the effect of heating rate on biomass pyrolysis product distribution.

(3) Experiments to help design a high-pressure, continuous, free-fall reactor for fast-hydropyrolysis of biomass.

All the experiments were performed with cellulose particles of 50 μm – 500 μm as representative of biomass particles. Cellulose particles were used to gain an early understanding of the complex reaction chemistry and products. Future work using lignin biomass particles has been planned.

### 1.1 Apparatuses to Allow Flow Visualization During Pyrolysis and Fast-Hydropyrolysis

Two apparatuses have been built that provide optical access during fast-pyrolysis and fast-hydropyrolysis of biomass. The first unit, described in Section 1.1.1, was a fast-pyrolysis reactor complete with product collection unit operations. Most parts of the reactor were made from quartz glass and allowed exploration of novel reactor designs and concepts. Results from these studies were used in the design of a high-pressure reactor. The second unit, described in Section 1.1.2, was a small-scale ablative reactor that was capable of precise heating control of biomass. The second unit was built to study the effect of heating rate and final temperatures on by-product formation (char) using a high-speed camera. A third unit was built, Section 1.1.3, to measure particle velocities at ambient conditions. Data from unit experiments with these apparatuses are being used to design and build an appropriate high-pressure hydropyrolysis reactor. Results and discussion are located in Section 1.2.

### 1.1.1 Optically Accessible Glass Fast-Pyrolysis and Fast-Hydropyrolysis Reactor

An optically-accessible, atmospheric-pressure, bench-scale, quartz/glass reactor system for pyrolysis under different heating rates was built. Details of the apparatus are described next. Three sets of experiments were completed in an attempt to optimize flow patterns at the entrance of the reactor (Section 1.2.1) and to increase biomass heating rates within the reactor, Sections 1.2.2-3.

**Description of Apparatus**

A process flow diagram (PFD) of the low-pressure pyrolysis reactor arrangement is shown in Figure 1.1. Two pictures of the biomass low-pressure reactor are shown in Figure 1.2. The bench-scale arrangement was composed of a magnetically-driven screw feeder connected to a series of quartz and borosilicate parts. The parts included the screw feeder, the reactor, the connector between the screw feeder and the reactor, a tar/char collector, a condenser with a liquid collection flash, a transfer line between the reactor and the condenser, and a coalescing filter with collection flask to collect any bio-oil that bypassed the

condenser. The screw feeder was designed for system pressures up to 770 kPa and feed rates of solid biomass as low as 0.1 g/min and as high as 2 g/min.

The cold helium flow was fed from the top of the reactor along with cellulose from the screw feeder. A detailed view of cellulose particle discharge from the screw feeder to the reactor feed tube is shown in Figure 1.3. The discharged particles from the screw feeder were swept by the cold helium flow and carried downward to the reactor tube. The purpose of the helium was to keep the biomass near 25 °C until it reached the heating zone in the reactor to achieve fast-pyrolysis. At the top of the reactor a hot gaseous stream was introduced to heat the cellulose particles rapidly. Nitrogen gas was preheated to the desired temperature and was introduced into the quartz reactor from the side above the location where biomass was discharged through the reactor feed tube. The reactor itself was heated externally by heating tape to maintain the desired temperature throughout the reactor to achieve the highest carrier gas and biomass heating rates possible. Possible configurations and methods for introducing the hot gas into the reactor, as well as different types of reactors, were tested and are discussed in Section 1.2.1.
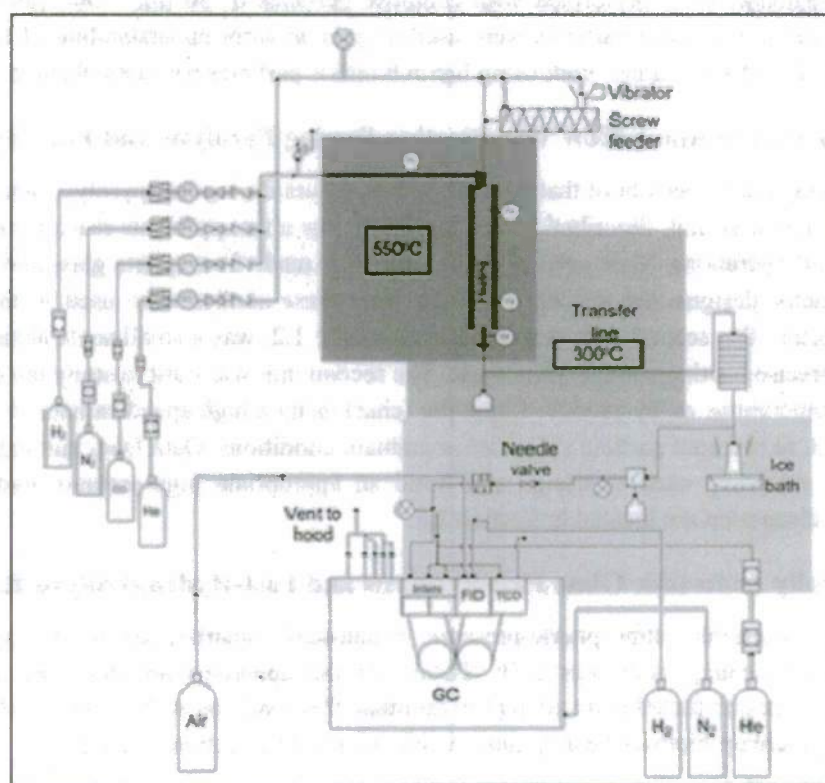


**Figure 1.1: Process flow diagram (PFD) for the low-pressure pyrolysis reactor**
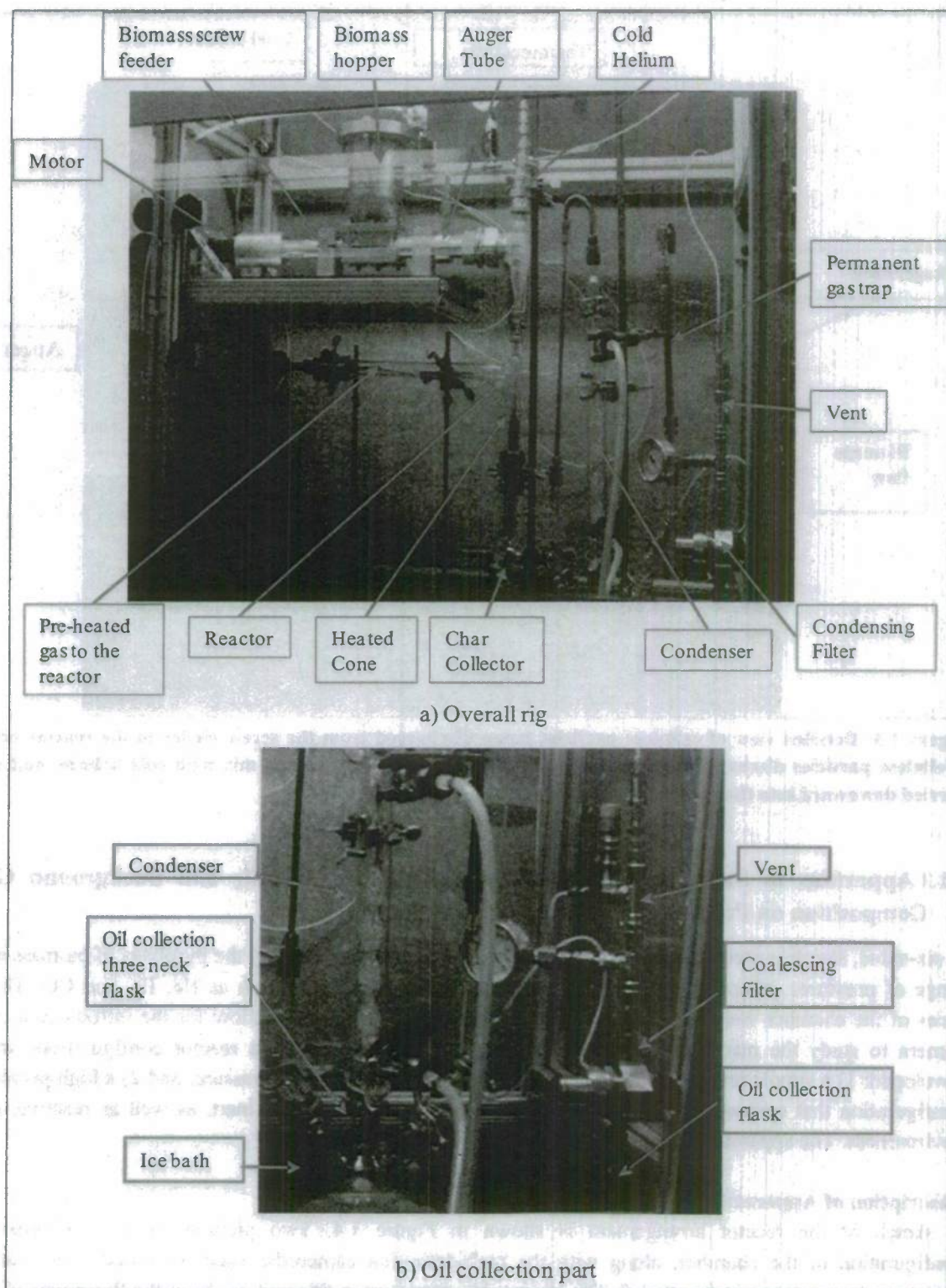
a) Overall rig



b) Oil collection part

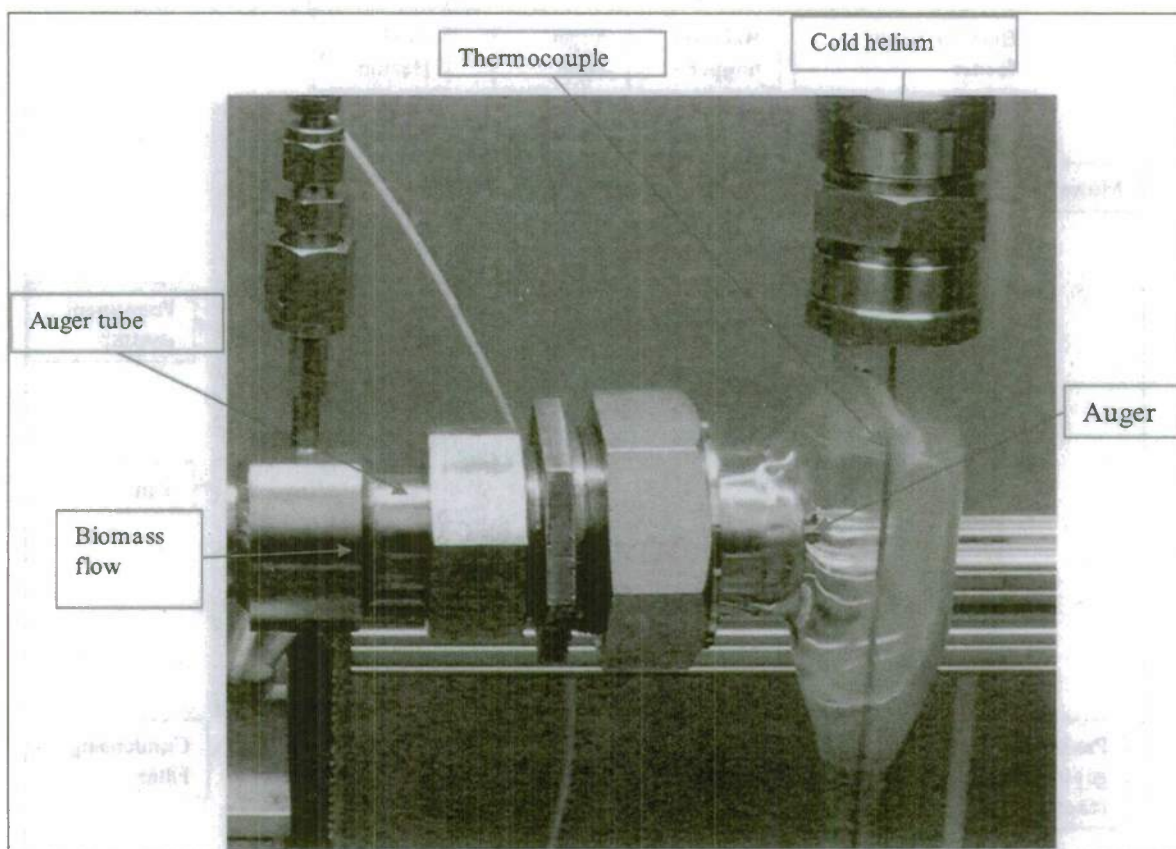**Figure 1.2: Assembled low-pressure reactor**

**Figure 1.3: Detailed view of cellulose particles being discharged from the screw feeder to the reactor tube. (Cellulose particles discharge from the screw feeder at the tip of the auger, mix with cold helium, and are carried downward into the reactor.)**

## 1.1.2 Apparatus to Study the Effect of Biomass Heating Profile and Background Gas Composition on Product Distribution (Pyroprobe)

A six-sided, stainless-steel, micro-reactor chamber was constructed to study the pyrolysis of biomass at a range of pressures, temperatures, heating rates, and gas environments such as He, $H_2$, and CO. Three faces of the chamber were designed to contain borosilicate viewports to allow for the introduction of a camera to study the macroscopic mechanism of pyrolysis. Two different reactor configurations were developed: 1) a simple arrangement for studies in an inert gas at 100 kPa pressure; and 2) a high-pressure configuration that enables the chamber to be pressurized to 6000 kPa in inert, as well as reactive, gas environment. The apparatus is described below.

**Description of Apparatus**
A sketch of the reactor arrangement is shown in Figure 1.4. Two pictures of the low-pressure configuration of the chamber, along with the high-definition camcorder used for initial visualization experiments are shown in Figure 1.5. The important component in this unit has been the Pyroprobe (CDS Analytical model 5200), which was connected through one of the side flanges and sat in the middle of the chamber, as seen in Figure 1.5 (bottom). The probe consisted of a resistively-heated platinum ribbon

attached to a 6.3 mm OD stainless steel tube. Rapid heating was achieved by applying voltage across the Pt ribbon. The biomass particle heating rate and final temperature could be controlled up to a maximum of 20 000 °C/s and 1400 °C respectively. In this arrangement, micro to milligram quantities of cellulose particles were placed on top of the platinum ribbon (width=2.1 mm, length=36 mm). The cellulose-particle-loaded Pt ribbon then was placed in the reactor chamber and heated rapidly at a predetermined rate in a suitable gaseous environment.

The gas supply servicing the Pyroprobe was routed to enter at the bottom of the reaction chamber so that it entered in a well-controlled and uniform pattern. After the chamber was flushed sufficiently to remove all of the air, the probe was fired, and the biomass was pyrolyzed in helium. The presence of the viewports on three faces allowed the camera to analyze the pyrolysis either from directly above the probe or from the side. Products, along with the sweep gas, exited the chamber from one of the sides and were vented to the hood. After all the product gases were swept out, the chamber was opened and cleaned, and biomass was re-loaded.

The reactor allowed visualization studies using a high-speed camera (Photron 1024PCI) capable of recording 1000 frames per second (fps) at 1 megapixel resolution. For heating rates of 1000 °C/s and above, a conventional 30 fps camera was found to have inadequate temporal resolution to give meaningful results.
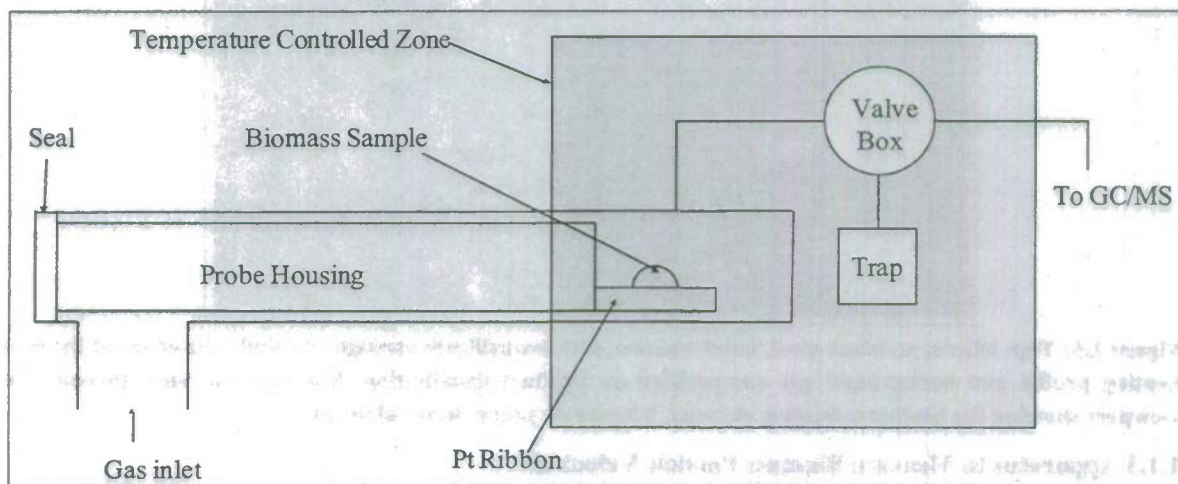


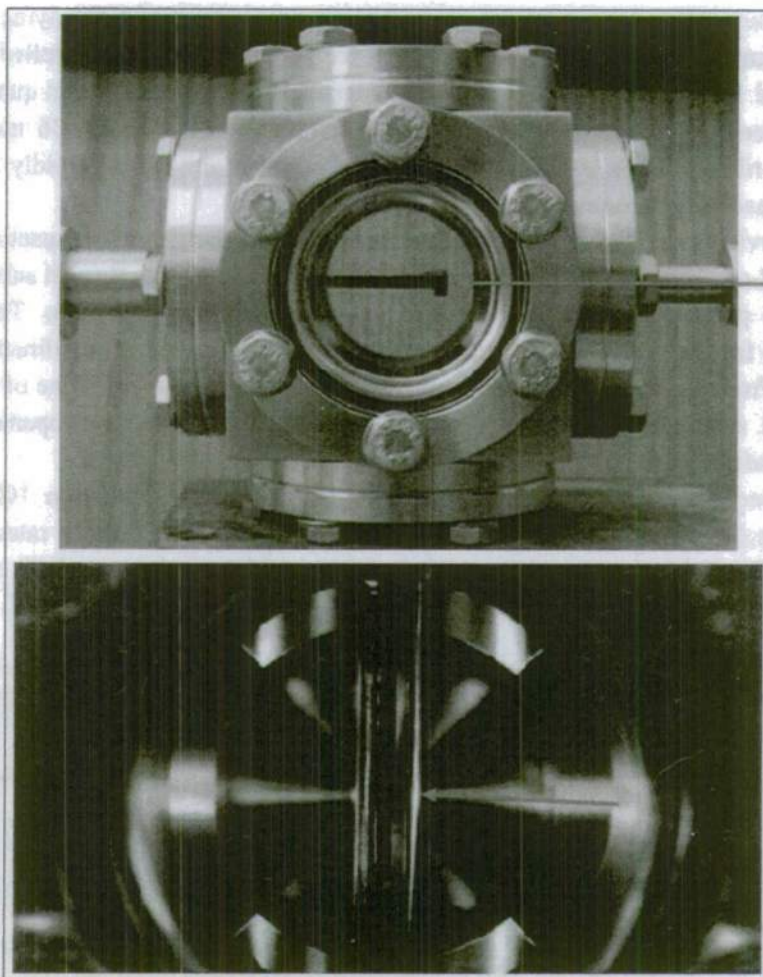**Figure 1.4: Schematic of the reactor arrangement.**

**Figure 1.5:** **Top: Micro, stainless-steel, batch reactor with borosilicate viewport to study the effect of biomass heating profile and background gas composition on product distribution. Bottom: Top view through the viewport showing the platinum heating element. The arrow points to the element.**

### 1.1.3 Apparatus to Measure Biomass Particle Velocities

In order to size the free-fall, high-pressure, hydropyrolysis reactor properly, determination of biomass particle velocities was deemed necessary. For this purpose a simple apparatus was built, as described below. Based on the experimentally-determined particle velocity, it was possible to calculate the extent of particle agglomeration that occurred while feeding the biomass using the custom screw feeder. The apparatus was tested using purified cellulose as feedstock at ambient conditions. The results from the experiments are shown in Section 1.2.2.

The apparatus consisted of a 2.5 cm transparent glass tube that was connected below the biomass screw feeder, as shown in Figure 1.6. The other end of the glass tube was attached to a vessel to collect the falling biomass. A reference scale, showing height in inches, was mounted next to the glass tube. An appropriate dark-colored background was mounted behind the arrangement. A high-definition 30 fps camcorder (Canon VIXIA HFS100) was used to record video during the experiment that lasted typically three minutes. The video then was analyzed frame-by-frame to visualize the movement of the cellulose particle agglomerates falling through a distance of 38-51 cm. This information allowed calculation of the

particle velocity for a certain number of particles that allowed determination of the average particle velocity. The extent of particle agglomeration was estimated through a comparison of the average particle velocities determined from the experiments and terminal velocities calculated as a function of particle size, using single-particle dynamics.
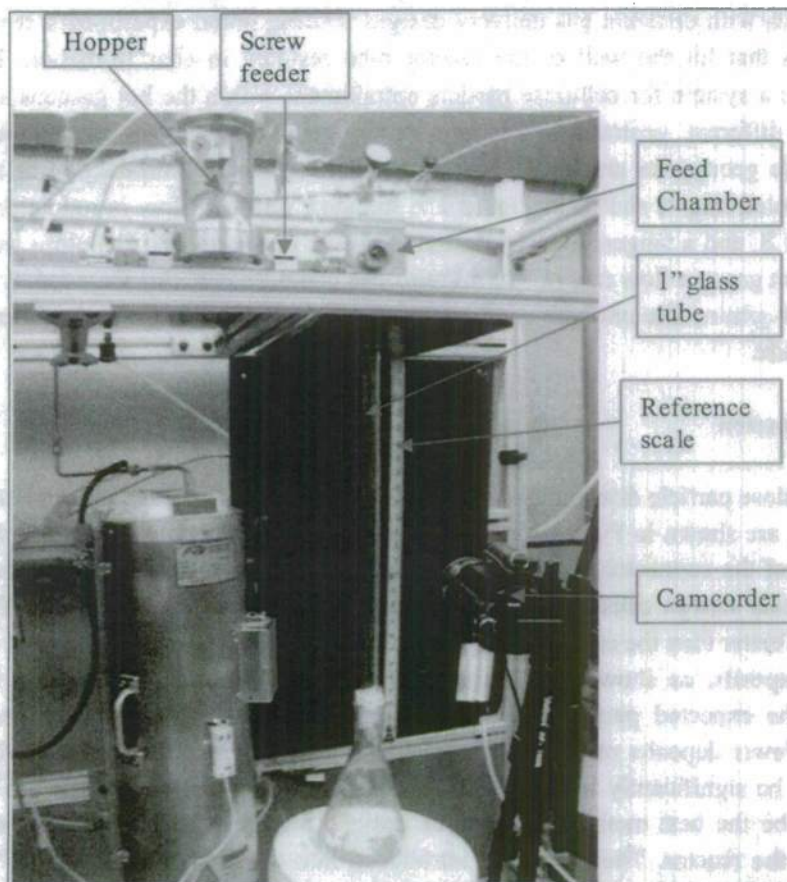


Figure 1.6: Photo of the experimental setup used for the determination of particle velocities.

## 1.2 Optimize Flow Characteristics for Desirable Transport Properties during Fast-Hydropyrolysis

### 1.2.1 Experiments Using the Optically-Accessible, Glass Pyrolysis Reactor

Three different studies were performed using the optically-accessible, glass reactor system, presented in Section 1.1.1, to help develop a pyrolysis reactor that provides fast, >1000 °C/s, heating of biomass. For some cases, modifications to the apparatus were made in order to try different pyrolysis reactor configurations.

### 1.2.1.1 Flow Optimization of Inlet Carrier Gas and Biomass to the Reactor

Discharged cellulose particles from the screw feeder were swept by a cold helium flow and carried downward to the reactor tube. At the top of the reactor tube, a hot gaseous stream was introduced to heat

the cellulose particles rapidly. The hot gaseous stream was introduced into the reactor in such a way that the cellulose particles remained entrained in the center of the reactor tube. This feature had two advantages. First, premature reactions and char formation were avoided by minimum cellulose in proximity to the wall. Second, rapid reaction and maximum pyrolysis were promoted by rapid heat transfer from the cone surface. Cold gas flow was used to mimic the hot gas flow to allow an examination of the flow patterns with different gas delivery designs. During initial experiments, it was observed that cellulose particles that hit the wall of the reactor tube resulted in char formation. It was, therefore, essential to design a system for cellulose particle entrainment within the hot gaseous stream away from the wall. Three different geometries for introducing cellulose particles in the reactor tube were investigated. These geometries are shown in Figure 1.7-1.9. Annular introduction of the preheated gas through a multi-holed ring is shown in Figure 1.7. Inclined, opposed flow introduction without swirl is shown in Figure 1.8, and a tangential swirl design is shown in Figure 1.9. Cellulose was co-fed into the reactor with helium gas at a flow rate of 750 ml/min. The cellulose particles were fed by a screw feeder at a flow rate of 0.18 g/min. The nitrogen gas flow rate was about 500 ml/min and was introduced into the reactor from the side.

**Results and Discussion**

Snapshots of cellulose particle distributions within the reactor using the annular design at times of 1 and 3 min, respectively, are shown in Figure 1.10 a) and b). Some of the cellulose particles dispersed radially, coating the walls of the connector. The buildup of cellulose on the walls continued, as shown in Figure 1.10 b). The annular design caused significant deposition of particles on the wall. The opposed flow design performed better than the annular design. Finally, the tangential injector allowed an operation with minimum wall deposits, as shown in Figures 1.10 c) and d). This observation is recognized to be consistent with the expected performance of swirling-flow injectors that are commonly used in the aerospace field. Fewer deposits of cellulose were found near the top of the reactor where temperatures were expected to be significantly less than 500 °C. This result suggested that the gas being introduced tangentially may be the best method of the three designs for preventing biomass from charring in the upper portion of the reactor. The gas being introduced into the reactor with two 45° angle side arms (pictures not shown) from left and right sides of the reactor had similar effect on cellulose distribution as compared the tangential one. However, the cellulose particles were pushed slightly to the front and back sides of the reactor, i.e. perpendicular to the gas inlets.

**Conclusions**

It was found that, amongst the designs tried, the tangential introduction of the gas with the cellulose particles discharging in the center of the reactor tube resulted in the best particle distribution within the reactor tube. Particles were found to be confined mostly near the center of the tube. The contact between cellulose particles and the wall occurred further downstream in the reactor tube. At this location within the reactor, the temperatures are expected to be high enough to mitigate any clogging due to char formation. The multi-holed ring design for gas injection resulted in the worst particle distribution amongst the three designs described above. Experiments with this design resulted in deposition of cellulose particles near the upper walls of the reactor where char formation is likely to occur. The results of these experiments will facilitate subsequent designs of the high-pressure, fast-hydropyrolysis reactor.

**Figure 1.7: Design for introducing biomass to "pre-heated" gas in the reactor. Biomass enters the reactor from the 12.5 mm tube along with unheated carrier gas and, "to-be-preheated (i.e. cold in initial experiments) gas" enters into the reactor from the ring with holes facing downward.**
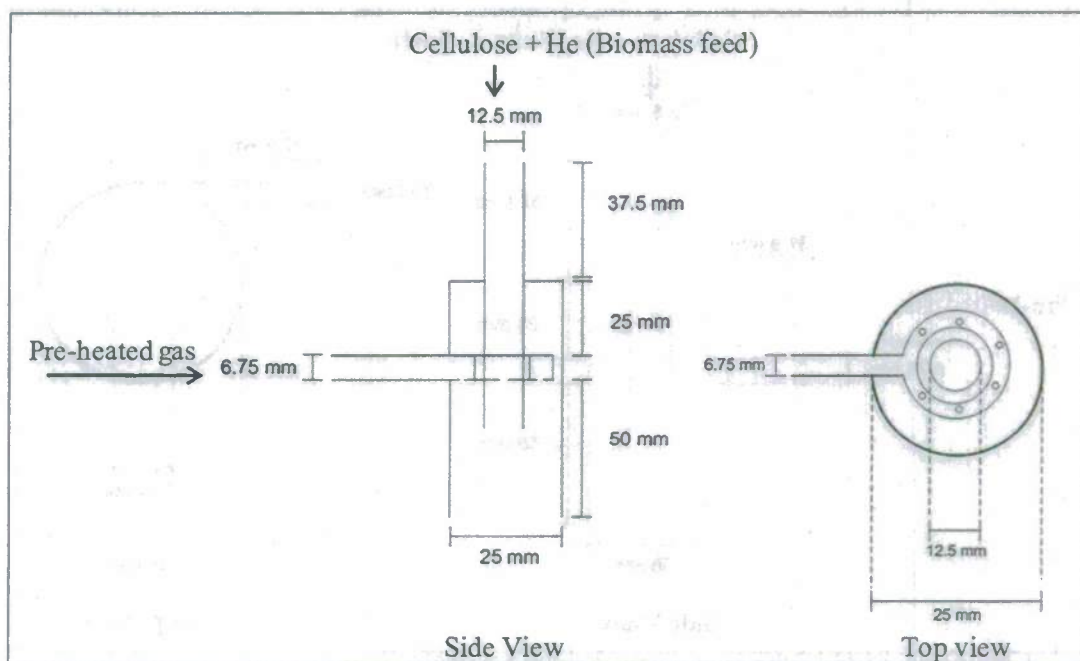


**Figure 1.8: Design for introducing biomass to "pre-heated" gas in the reactor. Biomass enters the reactor from the 12.5 mm tube along with unheated carrier gas, and "to-be-preheated gas" enters into the reactor from two 45 degree angle 6.75 mm tubes.**

Cellulose + He (Biomass feed)

12.5 mm

37.5 mm

37.5 mm

6.75 mm

37.5 mm

Pre-heated gas

25 mm

6.75 mm

25 mm

50 mm

12.5 mm

25 mm

25 mm

Side View      Top View

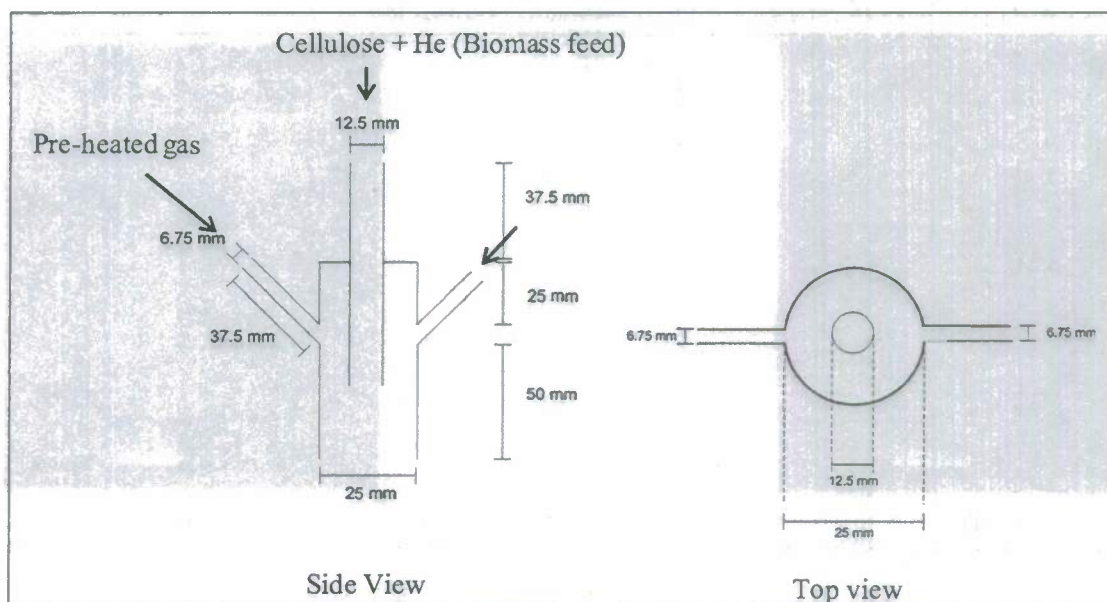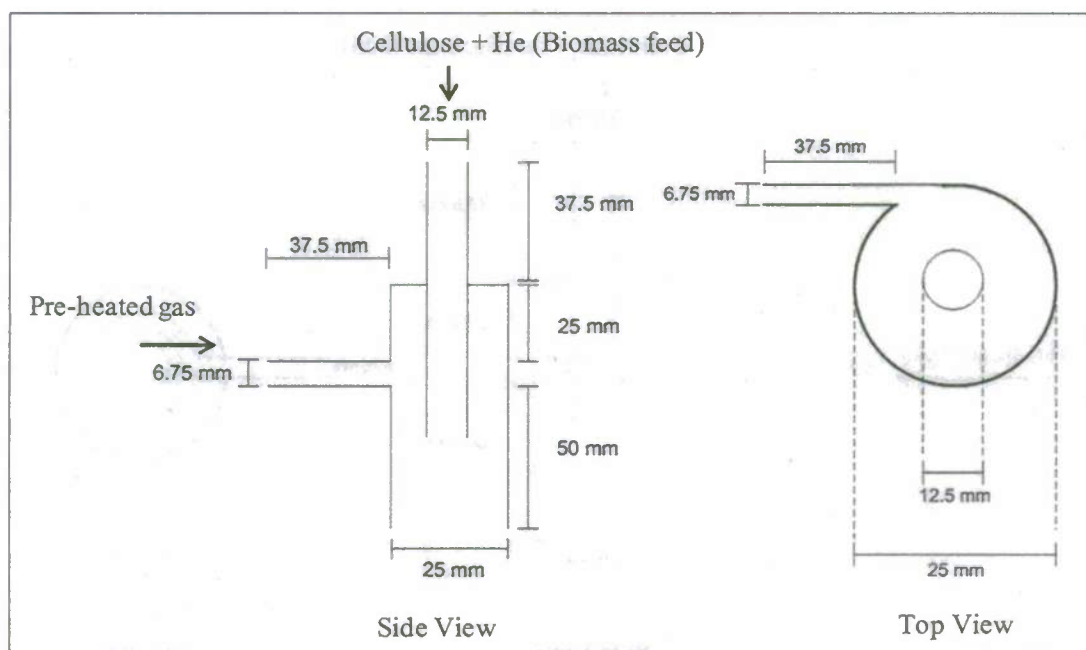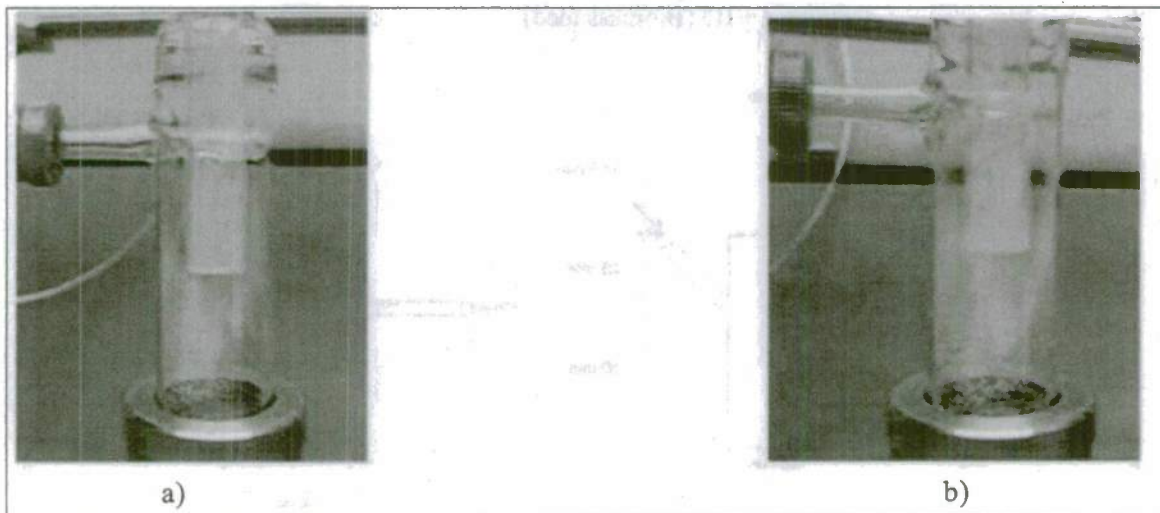**Figure 1.9: Optimal design for introducing biomass to "pre-heated" gas in the reactor. Biomass enters the reactor from the 12.5 mm tube along with unheated carrier gas, and "to-be-preheated gas" enters tangentially into the reactor from the 6.75 mm tube.**
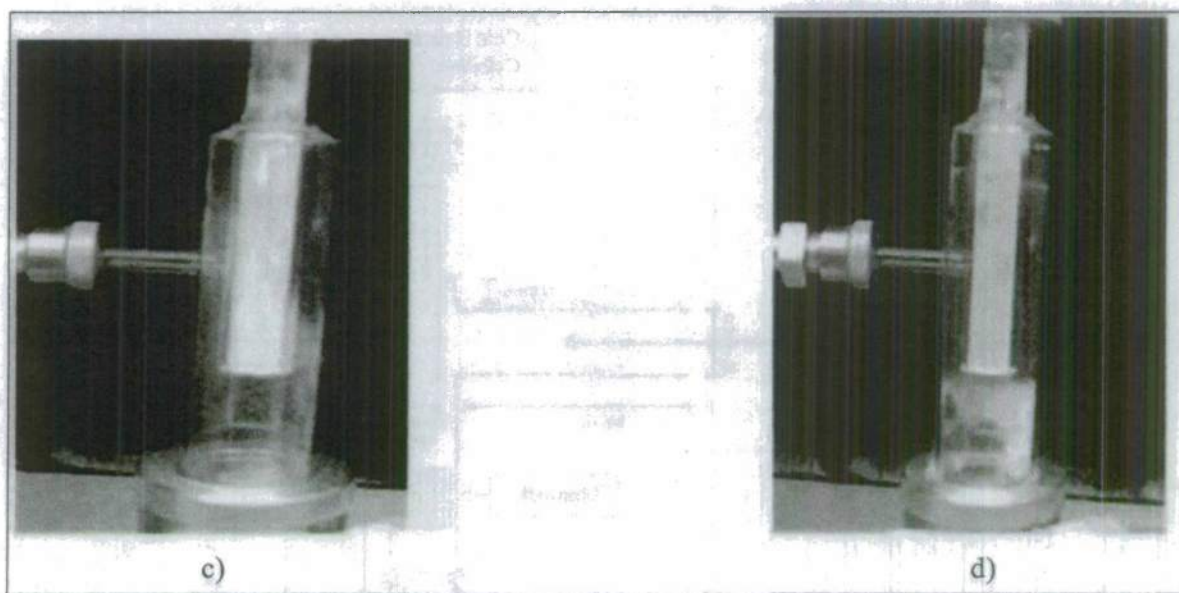


a)      b)

**Figure 1.10: Snapshots of two different hot gas feed configurations into the fast-pyrolysis reactor showing the distribution of cellulose at different times during operation: a) 1 min and b) 3 min, with the gas being introduced into the reactor using the ring design with holes facing down the reactor; c) 1 min and d) 3 min with the gas being introduced into the reactor using the tangential inlet design.**

### 1.2.1.2 Ablative Pyrolysis using an Indirectly–Heated, Catalytic Monolith

In this experiment, the hot gas, containing cellulose particles, traveled downward in the reactor tube and made contact with a cordierite-monolith, wash-coated with catalyst to heat the particles rapidly. The arrangement is shown in Figure 1.11. Ideally, the monolith performed two functions: ablative-pyrolysis of the biomass and catalytic-upgrading of oil immediately after vaporization. Here, a monolith without a catalyst loaded was tested to see if cellulose could be pyrolyzed ablatively using the monolith.

Commercially available purified cellulose with a mean particle diameter of 200 μm was used as a model biomass compound. Nitrogen entered the main reactor from the side and was preheated to 650 °C. The temperature in the reactor near the catalyst bed was about 600 °C. The rest of the reactor, tar/char collector, and transfer hose to the entrance of the condenser were heated to ~300 °C (Figure 1.2a). The cooling liquid on the cold side of the condenser was about -10 °C, and a three-neck flask was placed after the condenser in the ice bath to collect the bio-oil. A gas trap made with 30 cm long, 12.7 mm diameter stainless-steel tubing was placed after the 3-neck flask to collect the permanent (i.e. non-condensable) gas for GC analysis. The experiments were run for durations of 90 to 120 mins. After each experiment, the liquids formed and the solid residues were collected and weighed. The gas trap was stored in a refrigerator overnight to condense any bio-oil vapor. Then three samples of the trapped gas were analyzed using an Agilent 6890 gas chromatograph.

For these experiments, purified cellulose was used as a model biomass compound and was fed by the screw feeder at a flow rate of 0.18 g/min. Helium at room temperature was introduced along with the cellulose to keep the cellulose temperature less than 150 °C until it entered the reaction zone where the monolith was placed. A thermocouple was placed on the surface of the monolith to measure the surface temperature.
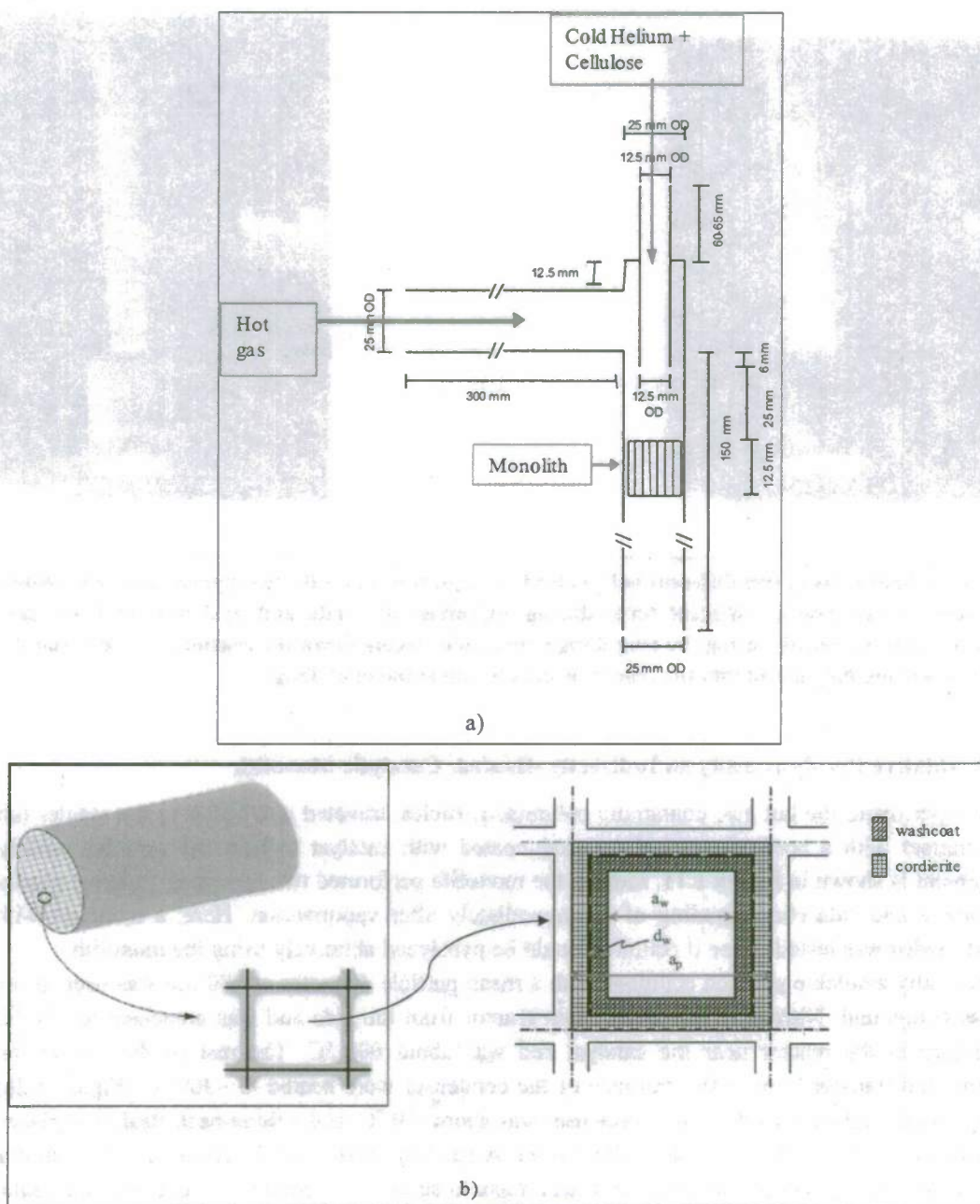
Figure 1.11: Schematic of: a) the quartz reactor with a cordierite monolith as the fixed bed; b) cross sectional view of the monolith and view of one monolith channel, $a_p = 1.43$ mm, $a_w = 1.13$ mm, $d_w = 1.1$ μm, where $a_p$ is the distance between the center of the two walls of a unit channel, $a_w$ is the width of the channel, and $d_w$ is the thickness of the catalyst washcoat.

## Results and Discussion

The mass balance results of a typical run are shown in Table 1.1. The char yield in most of the experiments was about 10% indicating that this reactor configuration was not pyrolyzing the cellulose completely. The yield of permanent gas was about 8%. The oil collected in the oil-collection flasks was

about 30 to 40%. Some oil that was produced during pyrolysis was trapped within the system and therefore not collected in the flasks. To account for this, the transfer lines and condenser were weighed before and after reaction to determine the mass of oil trapped in the system. The total mass balance was within 100±13% for all experiments.

Even at the lowest cellulose feed rates, the reactor eventually clogged due to the formation of char, which built up on top of the monolith. It is conjectured that the heat transfer rate from the reactor wall to the interior of the monolith was not sufficiently high for the required rapid heating of the cellulosic particles.

Table 1.1: Overall Mass Balance for the Monolithic Catalyst Reactor Study

| Cellulose Feeding Rate (g/min) | Reaction Time (min) | Cellulose Total Weight (g) | Char and Unreacted Cellulose (%) | Trapped Mass (%) | Gas Phase Percentage (%) | Bio-oil Collected (%) | Total Mass Balance (%) |
|---|---|---|---|---|---|---|---|
| 0.18 | 180 | 32.4 | 10.26 | 34.26 | 8.00 | 34.91 | 87.42 |

**Conclusions**

The experimental arrangements for feeding cellulose particles at the desired rate, pyrolyzing cellulose, and condensing and collecting oil pointed towards improvements necessary for future designs. The overall mass balance was within 100±13%; however, the reactor clogged frequently due to the formation of char, which built up on top of the monolith. These experiments also showed that a catalyst bed could not be inserted into the first section of the fast-hydropyrolysis reactor tube. Section 1.2.1.3 of this report describes experiments with ablative reactors that utilized a directly heated surface designed to improve heat transfer to the cellulose particles and reduce clogging.

**1.2.1.3 Directly Heated Ablative Reactor Studies**

As a part of the continued development of an ablative reactor, a new reactor was designed. Cellulose particles introduced into this reactor fell onto a heated, inclined surface in the shape of a cone. The cone, shown in Figure 1.12, was made of stainless-steel with a heating cartridge inserted in the cylindrical portion located below the cone. A type-K thermocouple was inserted about 1 mm in a 1.5 mm hole, which was located on one side of the tip of the cone. The cone, along with the heating cartridge, was placed in a 25 mm outer diameter quartz reactor. During the experiments small particles of cellulose were dropped onto the cone, along with a 750 ml/min helium flow, to keep the cellulose cool until it hit the cone. Another pre-heated 500 ml/min nitrogen flow (500-550 °C) was introduced in the reactor just above the cone to help maintain the surface temperature of the cone. A video was recorded by the 500 fps camera focused at the quartz reactor. Particle sizes were obtained by quantitatively comparing the particle dimensions with a reference dimension selected as the diameter of the thermocouple.

**Results and Discussion**

The transformation of micro-crystalline cellulose into oil vapor on the surface of the cone was observed using the high-speed camera. As an example, a series of frames tracking one cellulose particle with an initial diameter of 300 μm decomposing on the surface of the cone at 585 °C, is shown in Figure 1.13. In

this case, the irregularly-shaped cellulose particle became spherical as it was heated to the reaction temperature at time ~ 50 milliseconds. The semi-liquid particle decreased in diameter as outer layers vaporized between times of 50 and 70 milliseconds. After about 90 ms, the particle completely disappeared. The visualization study clearly showed the transition of cellulose particles through an intermediate liquid phase before vaporizing during pyrolysis. As observed by the naked eye, the small particles did not appear to leave a carbon residue on the surface after they were pyrolyzed. This result was very promising and showed that a heated surface is very effective for the pyrolysis of small cellulose particles without char formation.
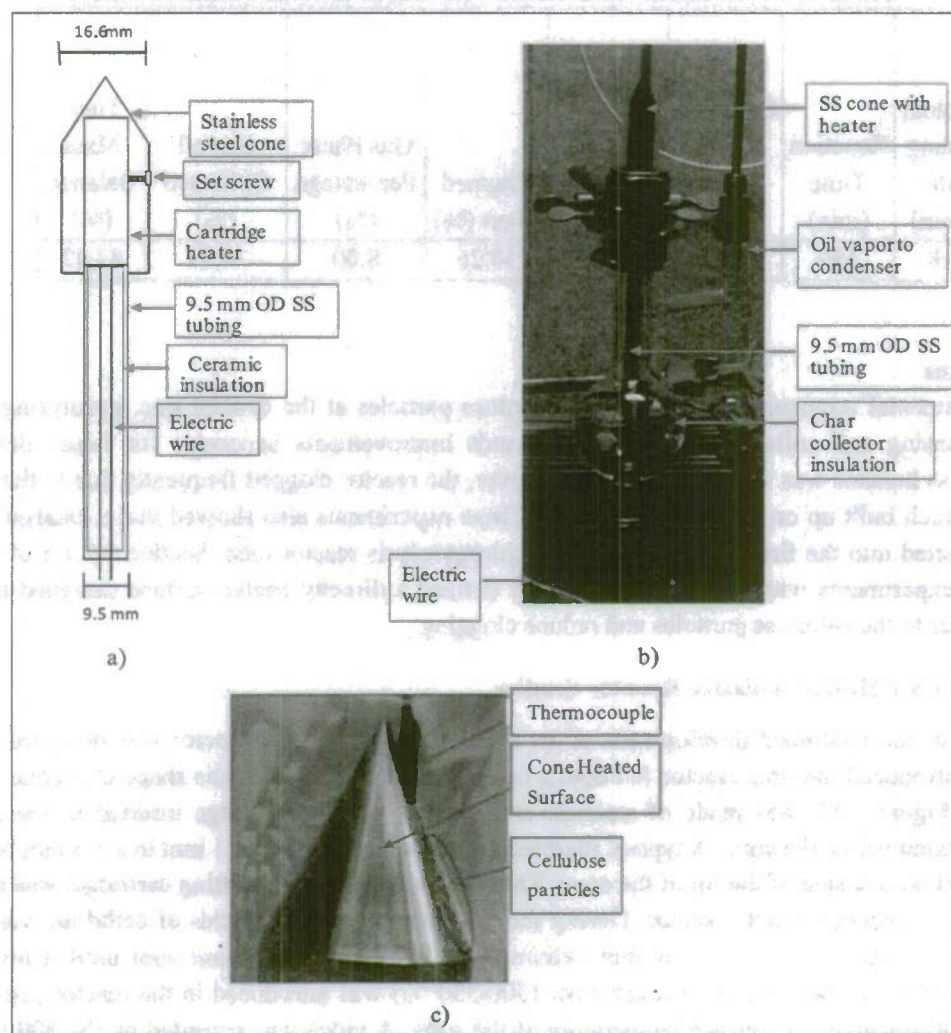


**Figure 1.12: Experimental setup of the heated, stainless-steel cone in the quartz reactor tube. a) schematic of the cone with cartridge heater inside and the feed through tube for electric connections; b) picture of the reactor setup; c) close up look of the cone in the reactor tube.**

The vaporization time depended on cellulose particle size and the temperature of the cone. In general, smaller particles and higher cone temperatures resulted in higher rates of particle vaporization. The relationship between vaporization time and cellulose particle sizes at 550 °C and 585 °C is shown in

Figure 1.14. For similar particle size, complete vaporization of cellulose particles at temperature of 550 °C was slower (up to 40-50% more time) than at 585 °C. The increase in time needed for complete vaporization with the increase in particle size indicated that heat transfer to the interior of the particle might limit the decomposition reactions at larger sizes.
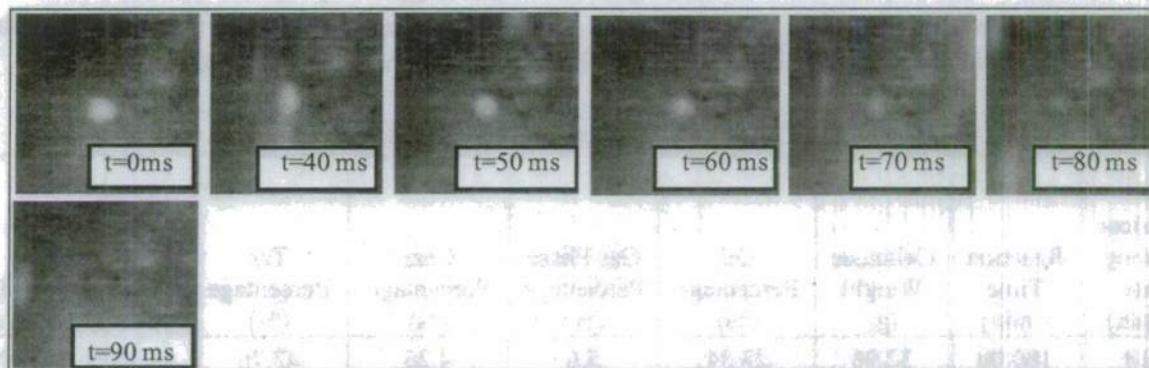


**Figure 1.13: Series of frames showing 300 µm cellulose particle vaporization as a function of time (2 ms frame⁻¹) in an inert atmosphere at cone temperatures of 550 and 585 °C.**
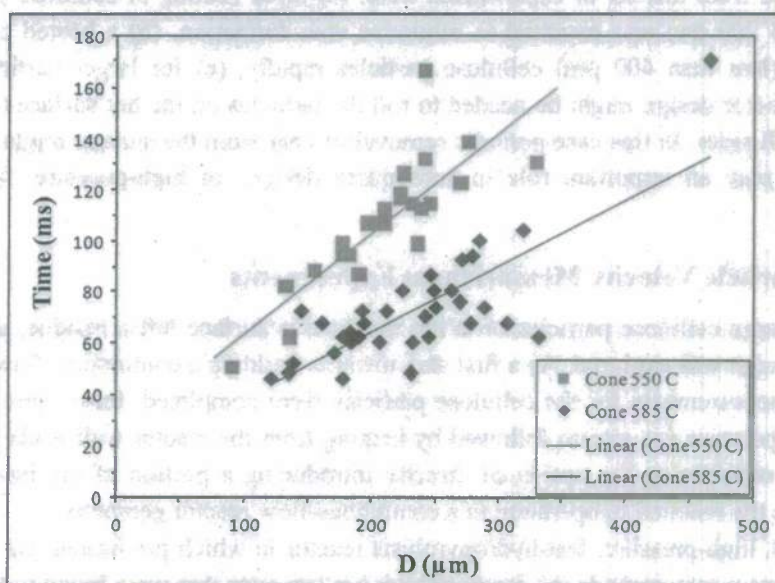


**Figure 1.14: Cellulose particle vaporization time as a function of particle diameter and cone surface temperature.**

In addition to the visualization experiments, the cone reactor was run for longer durations and the products were collected using procedures identical to those described in conjunction with the experiments in Section 1.2.1.2. Most experiments lasted for 60 to 180 min. The mass balance result of a typical run is shown in Table 1.2. The char yield in most of the experiments was 5-10%. The gas yield was 5-10%. The yield of collectable oil was 20 to 30%. About 25% of the oil produced during the pyrolysis process accumulated in the char collector and transfer line or exited with the permanent gases. The amount of oil

that accumulated in the system was estimated by weighing the individual pieces of equipment before and after the experiment. Using this procedure to estimate liquid holdup within the system, the overall mass balanced was closed to within a few percent. As with the monolith experiments, the reactor eventually clogged during the pyrolysis runs with the steel cone. The position of the cone relative to the cellulose feed tube was found to be important in terms of minimizing clogging. When the cone was placed at only 12.5 mm from where the cellulose was discharged, the reactor clogged very rapidly, typically within 1 h. When the cone was placed a little lower, e.g. about 38 mm from where the cellulose was discharged, the reactor usually did not clog within 1 h. The runs with this configuration typically lasted for about 3 h.

Table 1.2: Overall Mass Balance for the Cone Reactor Study

| Cellulose Feeding Rate (g/min) | Reaction Time ( min) | Cellulose Weight (g) | Oil Percentage (%) | Gas Phase Percentage (%) | Char Percentage (%) | Tar Percentage (%) | Oil Produced but Non-Collectable (%) | Total (%) |
|---|---|---|---|---|---|---|---|---|
| 0.18 | 180.00 | 32.96 | 28.34 | 5.6 | 4.25 | 43.76 | 22.76 | 98.57 |

### Conclusions

The lessons learned from this set of experiments were: (a) rapid heating of cellulose particles (25 °C to ~500 °C in 100 to 200 ms) was essential to minimize char formation, (b) a heated conductive surface could heat small (less than 400 μm) cellulose particles rapidly, (c) for larger particles or clusters of particles, a new reactor design might be needed to roll the particles on the hot surface to increase heating of particles from all sides. In this case periodic removal of char from the surface might be needed. These observations will play an important role in subsequent designs of high-pressure, fast-hydropyrolysis reactors.

### 1.2.2 Biomass Particle Velocity Measurement Experiments

Since heating of large cellulose particles on a hot conductive surface left a residue, a continuous-flow, free-fall reactor design was explored. As a first step towards building a continuous–flow, free-fall reactor, particle velocity measurements for the cellulose particles were completed. Introduction of particles in a relatively low temperature gas stream followed by heating from the reactor wall leads to char formation; therefore, we are considering the option of directly introducing a portion of the incoming gas stream preheated to above the reaction temperature in a continuous-flow reactor geometry.

A continuous-flow, high-pressure, fast-hydropyrolysis reactor in which pre-heated gas is mixed properly with unheated biomass may provide the required high heating rates that were found to be critical for high conversion of biomass to liquids. The reactor consisted of biomass falling under gravity in a heated reactor co-currently with preheated gas that provides the convective heating to the biomass particles. In order to estimate particle heating rates, and therefore the reactor length needed for complete biomass conversion, the average particle velocity for a given feedstock needed to be determined. Particle velocity experiments were carried out using the apparatus described in Section 1.1.3 (Figure 1.6) in order to measure the extent of cellulose particle agglomeration occurring while feeding cellulose using the screw feeder. Both "as is" cellulose and pre-dried cellulose particles were tested. The results, presented below, have been identified to be useful in future designs of continuous pyrolysis reactors.

**Results and Discussion**

The continuous-flow experiments were performed using commercially obtained purified cellulose sieved to a particle size of 50 μm. Particle velocities were measured at two different flow rates of cellulose particles, 0.1 and 0.5 g/min, with both "as is" cellulose and cellulose that was dried in a convection oven heated to 140 °C for 5 h. Drying the cellulose resulted in 3.8% reduction in weight, presumably due to the loss in water content. The cellulose then was transferred immediately to the screw feeder hopper and purged with dry nitrogen. For each experiment 10 representative velocity measurements were taken for each condition. Using the measured particle velocities, an effective particle size could be calculated using well-known single-particle dynamics[1] to determine the extent of particle agglomeration.

As an example, Table 1.3 shows a complete set of data collected for "as is" cellulose fed at 0.1 g/min which had an average particle velocity of 70±3.3 cm/s. It is possible to back-calculate the "effective" particle size based on the calculated particle velocity using single-particle dynamics[1]. At the conditions of these experiments, the "effective" particle size calculated was 230 μm; hence, it was deduced that there was an agglomeration of particles, and the "effective" particle size is about 4.5 times that of the particles without any agglomeration (50 μm).

The results of all the velocity measurement experiments are summarized in Table 1.4. Increasing the cellulose flow rate by a factor of five had only a small effect on particle velocities, increasing measured velocities by 7.6 cm/s, just outside the margin of error. The results from dried cellulose showed that the particle velocities were well within experimental error of the results for the "as is" cellulose. These results seemed intuitive because the weight loss due to drying was not substantial enough to have an effect on the agglomeration of the particles which, in-turn, affected their particle velocity.

For the following reaction conditions, reactor OD of 2.5 cm, total gas (He/$H_2$) flow rate of 15 l/min at 6800 kPa and 500 °C, cellulose feed rate of 0.5 g/min, and cellulose particle size of 50 μm, the calculated particle velocity was about 70 cm/s. For the same conditions, the time required to heat the particles to 500 °C was calculated to be about 0.3 s. A length of 60 cm was found to provide sufficient residence time (0.85 s) for complete conversion of the particles.

Table 1.3. Data Collected for 0.1 g min$^{-1}$ Undried Microcrystalline Cellulose

| Sample No. | Frames | Distance Travelled (cm) | Particle Velocity (cm/s) |
|:---:|:---:|:---:|:---:|
| 1 | 18 | 43.2 | 71.9 |
| 2 | 19 | 45.7 | 72.1 |
| 3 | 17 | 40.6 | 71.6 |
| 4 | 18 | 45.7 | 76.2 |
| 5 | 20 | 45.7 | 68.6 |
| 6 | 20 | 45.7 | 68.6 |
| 7 | 19 | 45.7 | 72.1 |
| 8 | 22 | 48.3 | 65.8 |
| 9 | 21 | 45.7 | 65.3 |
| 10 | 21 | 48.3 | 68.8 |

Table 1.4. Particle velocity and Effective Particle Sizes

| Condition of Biomass | Mass Flow of Cellulose (g/ min) | Average Particle Velocity ± Sample Standard Deviation (cm/s) | Effective Particle Size (μm) |
|---|---|---|---|
| Wet | 0.1 | 70 ± 3.3 | 230 |
| Wet | 0.5 | 77.5 ± 6.9 | 250 |
| Dry | 0.1 | 68.3 ± 4.8 | 220 |
| Dry | 0.5 | 76.7 ± 5.3 | 250 |

**Conclusions**

In summary, the agglomeration of micro-crystalline cellulose particles was found to have a weak dependence on mass flow rate but did not depend appreciably on the small reduction in moisture content due to drying of the "as is" cellulose particles. Using the above mentioned data along with a simple heat transfer calculation, a residence time of ~0.85 s (reactor length of 61 cm) was decided to be suitable for complete conversion of cellulose particles.

## 1.3 Use of Water Gas Shift (WGS) Catalysts in the Fast-Hydropyrolysis Reactor

Due to technical hurdles associated with construction of a fast-hydropyrolysis reactor that were initially unaccounted for, Task 1.3 was not started during the year one project period. Task 1.3 has been proposed and accepted as a part of follow on funding.

## 1.4 Use of WGS Catalysts in the Secondary HDO Reactor

Due to technical hurdles associated with construction of a fast-hydropyrolysis reactor that were initially unaccounted for, Task 1.4 was not started during the year one project period. Task 1.4 has been proposed and accepted as a part of follow on funding.

## 1.5 References

[1.1] M. Rhodes, *Introduction to particle Technology*, 2008, New York: Wiley.

## 2.0 Optically Accessible Gasifier

The optically accessible gasifier team has focused on the design and construction of an experimental gasifier including $H_2$ addition and optical viewports for quantitative measurements of the reaction and flow patterns.

### 2.1 Design of Experimental Arrangement

### 2.1.1 Description of Gasification Process

Gasification is the process in which solid fuels are converted into combustible gases. Carbon ($C_{(s)}$) is converted into carbon monoxide (CO) when reacted with steam ($H_2O$) at high temperatures and pressures. This CO release is accompanied with a release of hydrogen ($H_2$). Coal-steam gasification is an endothermic reaction process. In commercial gasifier units, heat for the reactions often is obtained by reacting excess coal with pure oxygen. The combustion process produces large amount of $CO_2$, and it is expensive to generate pure oxygen. It is beneficial to use non-carbon energy sources, such as solar and nuclear [2.2-2.3], to reduce carbon dioxide concentrations and to provide heat for the reactions. Carbon dioxide emission may be reduced further using hydrogen addition, which favors the reverse water gas shift reaction under gasification conditions [2.4].

The one step mechanism for the steam gasification reaction can be written as,

$$C_{(s)} + H_2O \longrightarrow CO + H_2 . \quad \Delta H = +131 \text{MJ/kmol}$$

The most important gas phase reaction is the water gas shift reaction,

$$CO + H_2O \rightleftharpoons CO_2 + H_2 . \quad \Delta H = -44 \text{MJ/kmol}$$
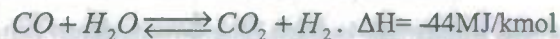
After the gasification process the mixture of gases contains CO, $H_2$, $CO_2$ and $H_2O$. The latter two species can be burned or used for liquid fuel synthesis [2.1].

Coal is mainly a mixture of carbon (>70%), hydrogen, oxygen, nitrogen, and traces of other elements. The abundance of coal in the United States and the high concentration of carbon make coal a promising fuel for large scale gasification processes. Reaction conditions such as temperature, pressure, particle size, and steam-to-coal ratio affect gasification residence times. A literature survey was conducted to determine the necessary operating conditions for the optically accessible gasifier.

### 2.1.2 Operational Temperatures

The steam gasification reaction has been found to be favored in the temperature range of 700 – 1100 °C [2.2-2.8]. The reactor was designed to operate with wall temperatures of 850 °C. This temperature value allowed the vessel to be made from stainless steel, which decreased both the time and cost required to build the reactor.

### 2.1.3 Operational Pressures

The steam gasification reaction is favored in the pressure range of 500 to 3000 kPa [2.2-2.8]. Commercial reactors operate at these pressures. An operating pressure of 1000 kPa was chosen for the reactor being built to facilitate cost effective material selection.

### 2.1.4 Coal and Steam Mass Flow Rates

The steam-to-coal ratio has been found to be an important parameter controlling the gasification process. Relevant literature indicated that excess steam could be used to decrease the residence time of the reaction [2.2, 2.3]. With excess steam the $CO_2$ concentration in the product gases has been found to increase. In the present design, a range of 2-3 was chosen for the steam to coal ratio. This range was chosen based on findings using the particle gasification model to reduce the required residence time while seeking to minimize the $CO_2$ concentration in the product gases. Based on the optimum steam to coal ratio, and the chosen coal flow rate of 0.4 g/s, the reactor was designed for a steam flow rate of 1.2 g/s. The operating conditions used for the design of the gasifier are listed in Table 2.1.

Table 2.1: Target operating conditions used during the design of gasifier

| Pressure (kPa) | Temperature ($^\circ$C) | Residence time (s) | Mass flow rate of coal (g/s) | Mass flow rate of steam (g/s) | External heat input (kW) |
|---|---|---|---|---|---|
| 1000 | 850 | 13 | 0.4 | 1.2 | 4.2 |

### 2.1.5 Reactor Design Parameters

The particle gasification model (described in section 2.3) was used to estimate a gasification time of 13.5 seconds for coal particles (50 microns) at a temperature of 850 °C, a pressure of 1000 kPa, and a steam-to-coal ratio of 2-3. A residence time on the order of 15 seconds was selected for the design to ensure that complete gasification of the coal was achieved. The dimensions of the reactor vessel were chosen to ensure this residence time.

It was assumed that the flow was isothermal, isobaric plug flow at steady state and that the particle can be modeled as a perfect sphere. Gravitational, buoyant and drag forces were considered. The drag force exerted by the steam was identified as the dominant force for particle motion. Consequently, the coal and the steam flows were designed to follow parallel paths to ensure the movement of the coal particles. A mean axial velocity profile was calculated based on the force balance. The terminal velocity of the coal particles was calculated based on a balance between the Stokes drag force (based on slip velocity between the particles and the steam) and the gravitational force. The relation used for terminal velocity is shown in Equation 2.1. $V_s$ is the terminal velocity, $\rho_p$ and $\rho_f$ indicate the particle and fluid densities respectively, $\mu$ is the fluid viscosity, $g$ is the gravitational acceleration, and $R$ is the particle radius.. The reactor length was selected to be 1.8 m based on the estimates of the terminal velocity of the coal particles and the selected residence times. The data used for determining the reactor dimensions is illustrated in Table 2.2.

$$V_s = \frac{2}{9}\frac{\left(\rho_p - \rho_f\right)}{\mu} g R^2 \tag{2.1}$$

Table 2.2: Velocity and length calculation for the reactor

| Input Data | Values |
|---|---|
| Coal mass-flow rate (g/s) | 0.4 |
| Steam mass-flow rate (g/s) | 1.2 |
| Pressure (kPa) | 1000 |
| Temperature (°C) | 850 |
| Coal density (g/cm$^3$) | 1.4 |
| Steam density (g/cm$^3$) | 0.002 |
| Steam inflow area (cm$^2$) | 45.6 |
| Velocity of steam initial (cm/s) | 13.2 |
| Velocity of coal initial (cm/s) | 0 |
| Coal particle initial diameter (μm) | 50 |
| Gravity (cm/s$^2$) | 981 |
| Ideal gas constant (J/mol-K) | 8.3145 |
| Viscosity of steam (N-s/cm$^2$) | $4.14 \times 10^{-9}$ |
| | |
| Velocity calculations based on Stokes flow | |
| $V_c$ (cm/s) (Particle velocity relative to steam) | 4.6 |
| Velocity for coal particle (cm/s) | 17.8 |
| Residence time (s) | 10 |
| Length of the reactor (cm) | 178 |

## 2.2 Experimental Arrangement

### 2.2.1 Summary of Design

The experimental arrangement chosen for studying the coal gasification process was based on the requirements summarized in section 2.1, and is described in the following. The gasifier vessel is constructed into separate spool pieces connected by flanges. Coal is fed into the topmost spool of the gasifier vessel using an auger-type feeder. High-temperature, high-pressure steam is also injected into the topmost spool of the gasifier vessel perpendicular to the coal feeder. The steam is generated by reacting hydrogen and oxygen external to the vessel. The chemical steam generator is designed to provide steam at the required temperatures and pressure. The gasifier vessel is heated externally using radiant heaters to provide additional energy for the gasification process. Ash is collected at the bottom of the gasifier vessel in a dome shaped collector. The product gas samples are collected at the gasifier vessel exit. Species concentrations and temperature values can be measured at various axial locations using tunable diode lasers. Optical access is provided using a specially designed windowed spool piece. The modular design of the gasifier vessel was chosen to allow interchange of the spool pieces. Detailed descriptions of the gasifier vessel and the four subsystems (steam generator, coal feeder, radiant heaters, and optical diagnostics system) are given in sections 2.2.3 – 2.2.7.

### 2.2.2 Status of the Optically Accessible Gasifier

The optically accessible gasifier and the heater, steam generator, and coal feeder subsystems have been assembled. Components for the optical diagnostics subsystems have been obtained. Installation and testing of the heater system has been completed. The coal feeder has been fabricated, and operational verification has been completed. The virtual instrumentation interface and the data acquisition system have been organized and programmed. Plumbing and assembly of the reactor and the steam generator have been completed.

### 2.2.3 Gasifier and Support Structure Assembly

The gasifier vessel assembly consists of the vessel, heater system, support stand, ash removal unit, and the hoisting system, as shown in Figure 2.1(a). The height of the reactor is 2.25 meters, and the overall height of the assembly is 2.5 meters. The internal diameter of the vessel is 7.5 cm. The vessel material, stainless steel (SS316H), has been chosen using the ASME Boiler and Pressure Vessel code for the target operating conditions (Table 2.1).

The gasifier vessel was designed to consist of three modular spool pieces fastened together. This design was selected to allow for the placement of the optically accessible spool at different locations along the length of the vessel. The hoisting system, consisting of a winch and pulleys, is expected to enable easy relocation of the optically accessible spool. The reactants are injected into the top of the gasifier vessel (Figure 2.1(b)). Exhaust gases are vented from the bottom-most section of the vessel. The coal and steam inlet ports are positioned perpendicular to each other to enhance mixing. Steam is injected tangential to the inner diameter of the reactor vessel to induce swirl in the flow.

The gasifier stand has been designed to support the weight of the entire structure and to provide a convenient method for removing ash without disassembly of the entire gasifier vessel. The support stand is assembled using two ANSI flanges rated for the operating conditions. The top flange is welded to the reactor spool, while the bottom flange is welded to a pipe end cap (Figure 2.2(a)). A tube (2.54 cm OD) with a slot facing the floor is inserted horizontally through the end cap to facilitate removal of the product gases with minimal entrainment of solid particles (Figure 2.2(b)). The solid waste is collected in the cap.

The vessel is instrumented to obtain temperature and pressure measurements along the length of the reactor. The gasifier is maintained at a constant temperature with the use of the OMEGA CRWS radiant heaters. The heaters are capable of operating at temperatures up to 975 °C.
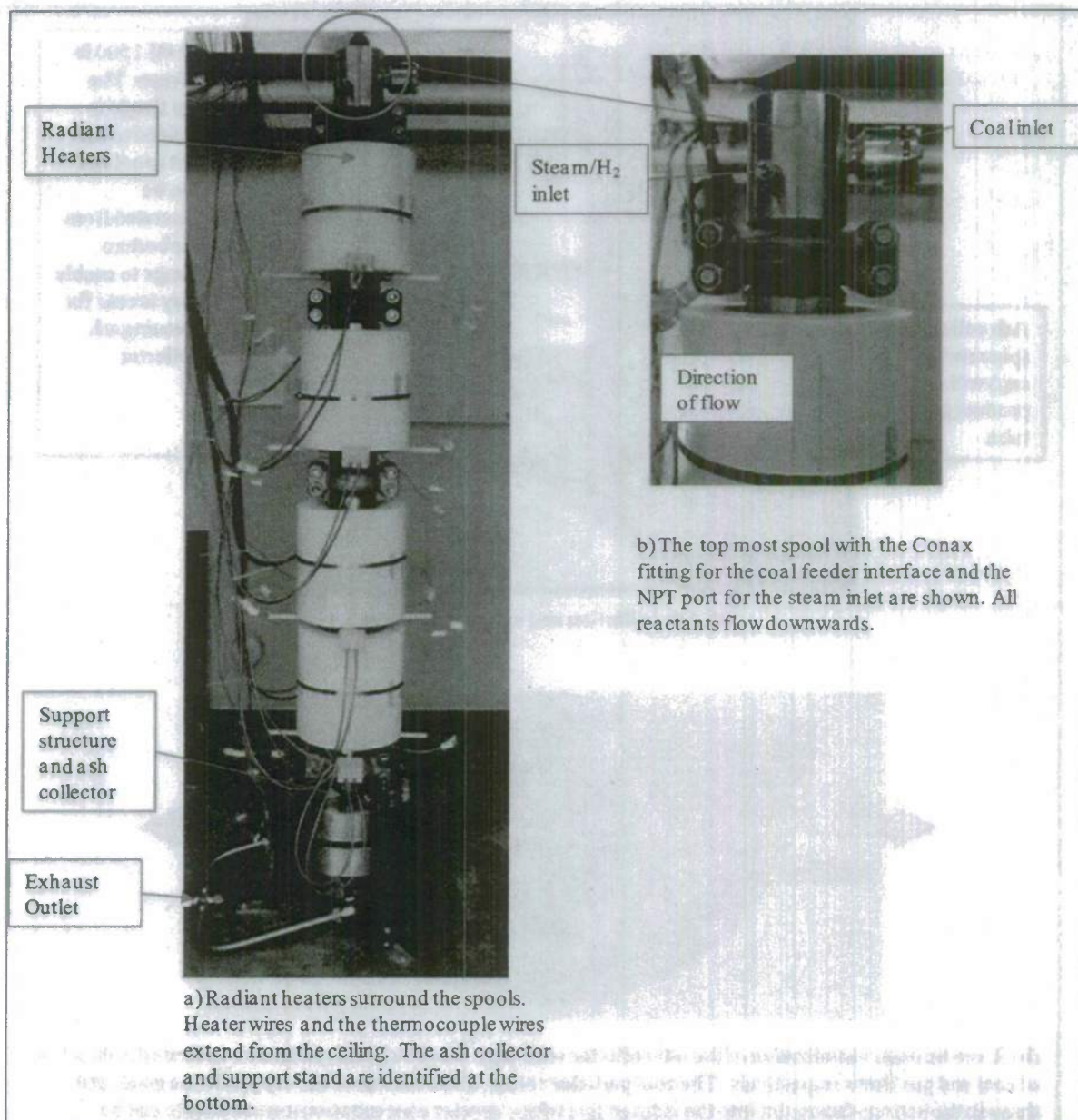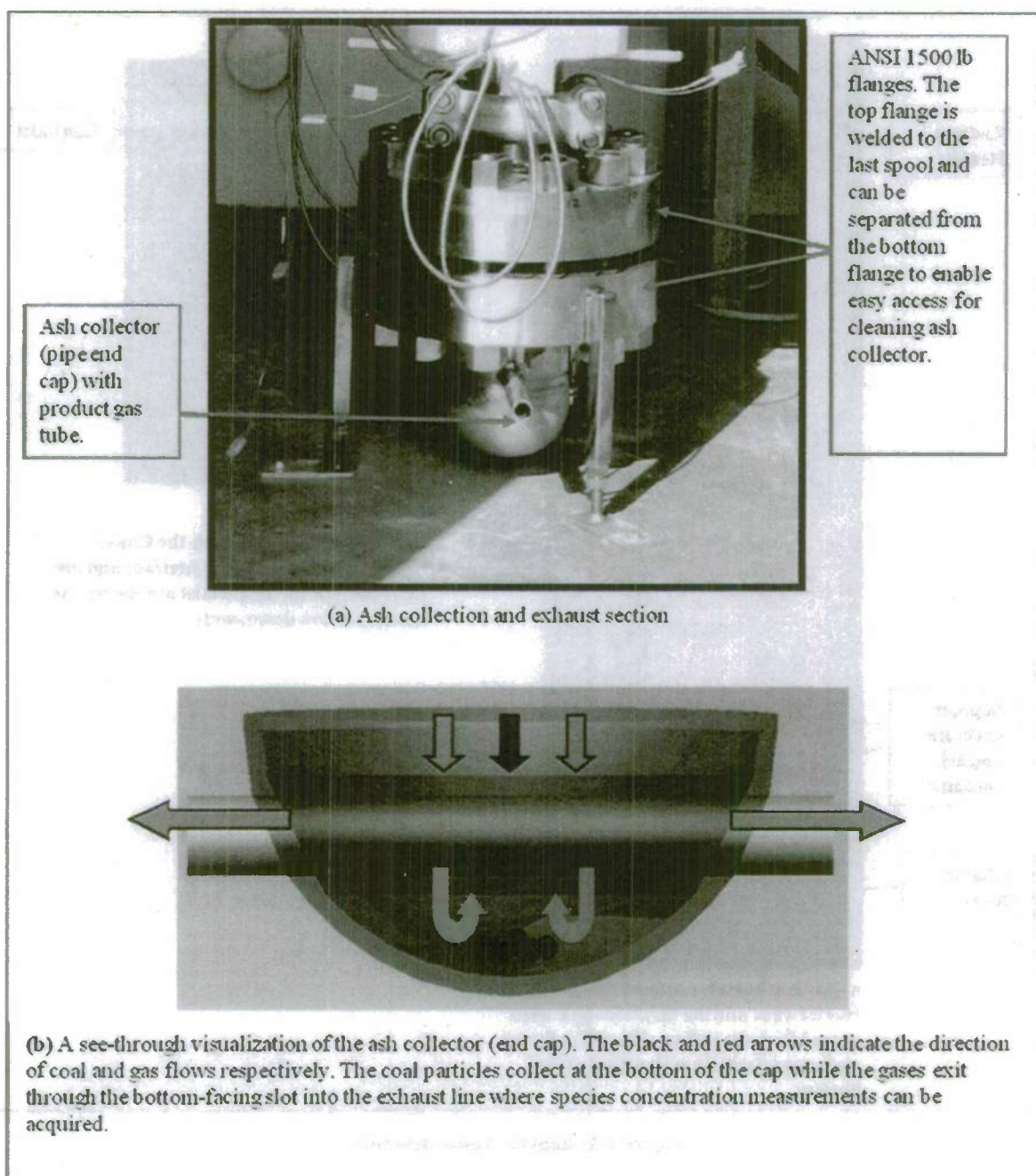
**Figure 2.1: Reactor vessel assembly**

ANSI 1500 lb flanges. The top flange is welded to the last spool and can be separated from the bottom flange to enable easy access for cleaning ash collector.

Ash collector (pipe end cap) with product gas tube.

(a) Ash collection and exhaust section



(b) A see-through visualization of the ash collector (end cap). The black and red arrows indicate the direction of coal and gas flows respectively. The coal particles collect at the bottom of the cap while the gases exit through the bottom-facing slot into the exhaust line where species concentration measurements can be acquired.

**Figure 2.2: Gas exit section**

Assembly of the gasifier has been completed.

### 2.2.4 Coal feeder system

An auger system was developed for feeding coal into the reactor. The feeder is shown below in Figure 2.3. It has been designed to operate for more than one hour at a pressure of 1000 kPa. Coal is stored in a hopper that is welded to the auger shaft. The auger rotates in the shaft, displacing the coal. The shaft is connected to the reactor using a CONAX fitting. Nitrogen is used to pressurize the system and to minimize the amount of steam entering the feeder. O-rings, placed around the shaft, are used for sealing the vessel. The auger is rotated using an electric servo motor acquired from Aerotech Inc. The speed and torque of the motor can be changed to allow variable coal feed rate during the operation of the reactor. The coal feeder is supported using a rope-pulley-counterweight system. This system allowed the feeder to move with the reactor to accommodate thermal expansion.
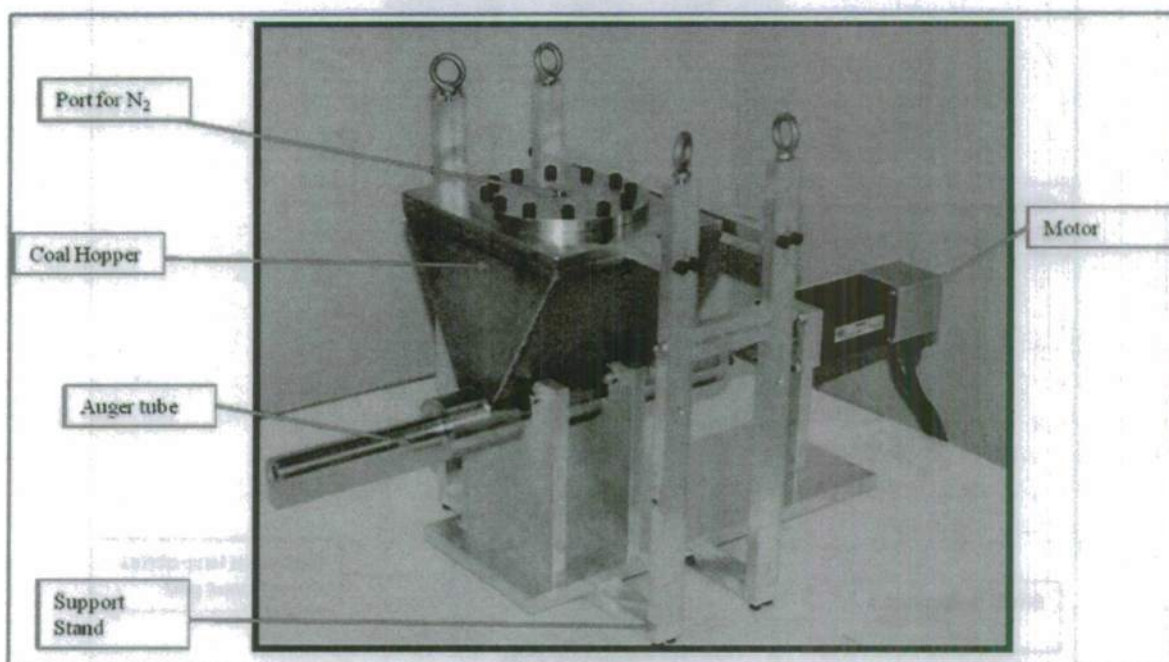


**Figure 2.3: Coal feeder system**

### 2.2.5 Steam Generation System

Steam is produced using a chemical steam generator at the temperatures and pressures required for the gasification process. The steam generator consists of four components: a casing, a cooling jacket, an insert plug, and a spark plug. Figure 2.4 shows the assembled steam generator. Hydrogen and oxygen enter the steam generator through ports on the side of the casing. The hydrogen flows in two channels within the generator: a sleeve flow and a core flow. This design allows reaction of the hydrogen to be distributed along the length of the steam generator and provides film cooling using unreacted hydrogen. The hydrogen channels also can be used to add excess hydrogen into the reactor. Computational results have indicated that excess hydrogen during the gasification process reduces carbon dioxide concentrations.

The adiabatic flame temperature of the hydrogen-oxygen combustion reaction is nearly 3000 °C. The water jacket ensures that the steam generator is not exposed to temperatures above the designed values. The temperature of the steam is reduced to 800 – 1100 °C in the water cooling section of the steam generator. In this section water at room temperature is injected into the flow. The materials selection has been performed based on temperature constraints of the steam generator. Nickel 625, Nickel 200, Hastelloy X, and Copper 101 have high melting points and are used in this high temperature application. Table 2.3 illustrates the material selection for the various components of the steam generator.
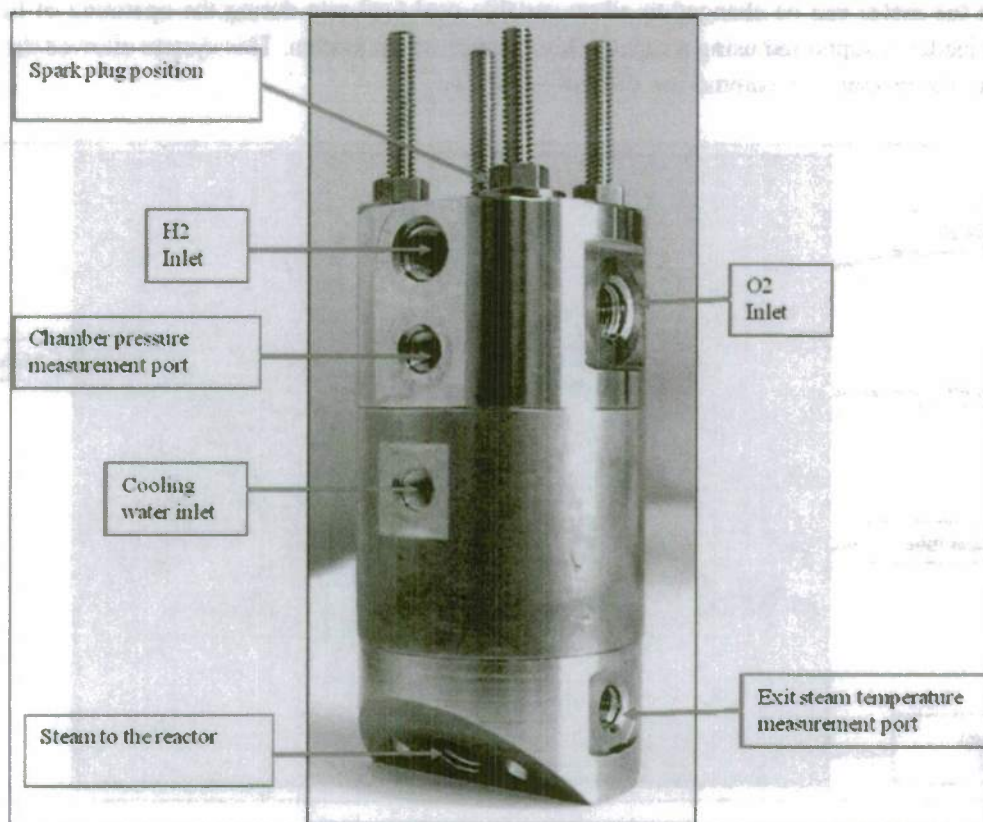


**Figure 2.4: Steam generation system**

Table 2.3 Material used for steam generator components

| Part | Material |
|---|---|
| Casing | Nickel 625 |
| Insert plug | Nickel 200 |
| Cooling Jacket | Copper 101 |
| Spark Plug | Inconel (Auburn I 33) |
| Metal Seals | Teflon coated metal |
| Steam Generator to Coal gasifier interface | Hastelloy X |

The assembly of the steam generation system has been completed.

## 2.2.6 Heater System

A radiant heater mounted on the gasifier vessel is shown below in Figure 2.5. A heater supplies 2.3 kW of energy until the set point for the wall temperature is reached. The heater controller then cycles power to the heater to maintain the wall temperature at the desired value. The heaters are rated for temperatures up to 975 °C. Four of these heaters, placed along the length of the vessel, are used for the entire reactor. Each heater unit is controlled individually based on the local reactor wall temperature.
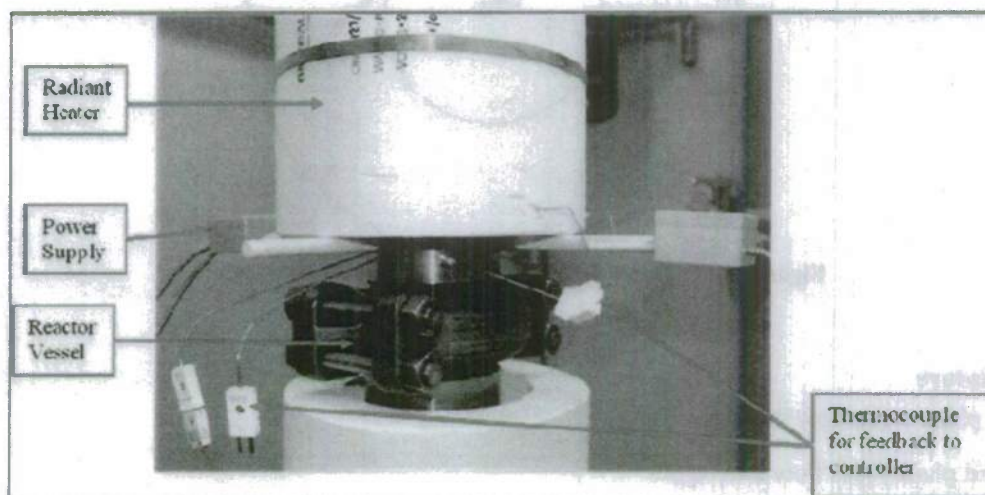


**Figure 2.5: Heater system**

The heater system assembly and testing have been completed.

## 2.2.7 Optical Diagnostics System

Tunable diode laser absorption spectroscopy measurements are employed to determine temperature values and species concentrations at various axial locations. A fused silica window is used for optical access. Lasers operated at wavelengths less than 2 μm are used to allow measurements of $CO$, $CO_2$, and $H_2O$ concentrations. Nitrogen is used to purge the windows to prevent accumulation of coal particles.

## 2.3 Modeling of the Gasification Process

### 2.3.1 Plug Flow Reactor Model

A plug flow reactor model was developed to simulate the physical and chemical processes that occur in a steam-coal gasifier. A one-film particle burning sub-model was used to determine the particle consumption rate and the net diffusion of steam at the surface of a coal particle. The water-gas shift reaction and the steam-coal gasification reaction were assumed to be at equilibrium. The sub-model of the particle was unified with a one-dimensional macro plug-flow reactor model [2.9]. Temperature values, species concentrations, and velocity profiles along the reactor height were obtained by solving the mass, momentum and energy conservation equations. Boundary conditions for the model were chosen to

replicate the experimental arrangement. Details of the particle burning sub-model [2.10] are described below. A schematic of the reaction process and diffusing species is shown in Figure 2.6.
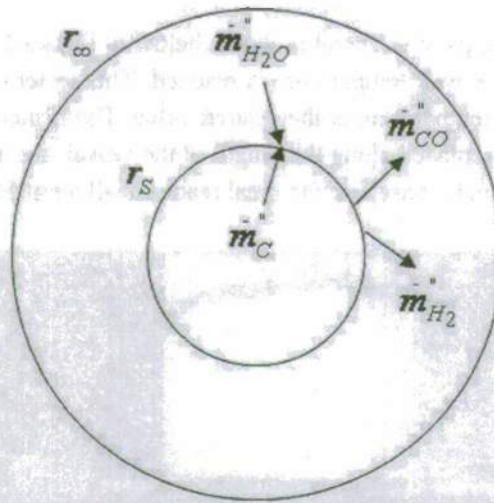


**Figure 2.6: Diffusion of steam at the surface of a coal particle.**

## Nomenclature

$\dot{m}_g$ - gas phase mass flow rate, kg/s

$\dot{m}_C$ - solid phase mass flow rate, kg/s

$\rho_g$ - gas phase density, kg/m$^3$

$\rho_C$ - solid phase density, kg/m$^3$

$\dot{m}_{C,burn}$ - burning rate of a single coal particle, kg/s

$\Gamma$ - net burning rate of coal in a control volume, kg/(m$^3$-s)

$d_p$ - diameter of coal particle, m

$A_T$ - cross-sectional area of reactor, m$^2$

$d_T$ - reactor diameter, m

$u_g$ - gas phase velocity, m/s

$u_C$ - solid phase velocity, m/s

$\varepsilon$ - solid phase volume fraction

$T_C$ - solid phase temperature, K

$T_g$ - gas phase temperature, K

$C_{pC}$ - solid phase specific heat capacity, J/(kg-K)

$C_{pg}$ - gas phase specific heat capacity, J/(kg-K)

$h_C$ - convection heat transfer coefficient, W/(m$^2$-K)

$\sigma$ - Stefan's constant, 5.67x10$^{-8}$ W/(m$^2$-K$^4$)

$\zeta$ - emissivity of coal particles

$\Delta H_{C-steam}$ - heat of reaction of coal-steam gasification reaction, J/mol

$H_{rxn,water-gas}$ - heat of reaction of water-gas shift reaction, J/mol

$\Delta \dot{n}_{co}$ - number of CO moles participating in water-gas equilibrium reaction, mol

$\dot{q}''$ - external electrical heat flux applied on reactor surface, W/m$^2$

$MW_C$ - molecular weight of carbon, kg/mol

$D_{H_2O-mix}$ - binary diffusion coefficient between the bulk gas stream and steam, m$^2$/s

$P$ - total pressure in control volume, Pa

$R_u$ - universal gas constant, J/(mol-K)

$k_s$ - coal-steam gasification rate constant, kg/(N-s)

$X$ - mole fraction

$Y$ - mass fraction

Assumptions used for the sub-model were as follows:

1. The process is quasi-steady.
2. The spherical carbon particle sublimates in a quiescent infinite medium that initially contains only steam.
3. No interactions with other particles occur.
4. The only surface reaction prevailing is: $C + H_2O \rightarrow CO + H_2$, $\quad k_s$
5. $H_2O$ diffuses inward and the products $CO$ and $H_2$ diffuse outward.
6. Pore structure and internal temperature gradient of carbon particle is negligible.

$$CO + H_2O \rightleftharpoons H_2 + CO_2, \quad k_p = \frac{X_{CO_2} X_{H_2}}{X_{CO} X_{H_2O}}$$
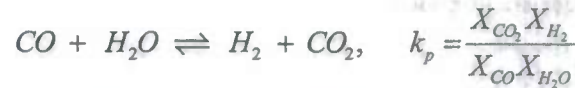
Based on the one-film model, the rate of coal particle mass consumption is:

$$\dot{m}_C = \dot{m}_{C,burn} = \frac{\pi d_p^2 k_s P_t D_{H_2O-mix} MW_C}{\left( \frac{k_s d_p R_u T_g}{2} + D_{H_2O-mix} MW_C \right)} Y_{H_2O_\infty}, \left( \frac{kg}{s} \right) \tag{2.2}$$

The mass flow rate of coal conversion per unit volume is,

$$\Gamma = N \dot{m}_{C,burn}, \qquad \left( \frac{kg}{m^3 s} \right) \tag{2.3}$$

where $N$ is the number of coal particles per unit volume.

The sub-model was unified with a one-dimensional macro plug-flow reactor model for a tubular reactor having a diameter of 7.75 cm and 1.75 m long. A mixture of coal and steam was specified at the inlet of the reactor. The gas phase mass flow rate of 1.5 g/s, and the solid phase flow rate of 0.5 g/s was used for most cases. A constant heat flux of 80 kW/m$^2$ was applied at the surface of reactor. A schematic of the control volume, used for calculations, is shown in Figure 2.9. The assumptions for the plug-flow reactor model are described below:

1. Steady state, one-dimensional.

2. Coal particle burning rate obtained from one-film particle model.

3. Water-gas shift reaction is in equilibrium with the coal-steam gasification.

4. Ash does not remain on the coal particle surface (unreacted core-shrinking model).

5. Solid and gas phase velocities are different.

6. Constant hydrostatic pressure.

7. Interactions between the coal particles are neglected due to a very dilute system.

8. Ideal gas equation of state is applicable.

9. The potential and kinetic energies have been neglected in comparison to thermal energy due to the high temperatures and relatively low velocities.
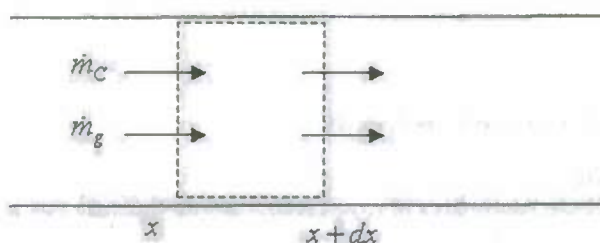


**Figure 2.7 Schematic of one-dimensional plug flow reactor.**

The mass and energy balances are given as:

$$\left.\frac{\dot{m}_g + \dot{m}_C}{A_T}\right|_{x=0} = \rho_g u_g (1-\varepsilon) + \rho_C u_C \varepsilon \tag{2.4}$$

Solid: $\dfrac{d}{dx}(\varepsilon \rho_C u_C) = -\Gamma$ $\tag{2.5}$

Gas: $\dfrac{d}{dx}((1-\varepsilon)\rho_g u_g) = \Gamma, \quad \dfrac{kg}{m^3 s}$ $\tag{2.6}$

Solid: $\dfrac{d}{dx}(\varepsilon \rho_C u_C C_{pc} T_C) = N_C \pi d_p^2 \left[ h_C (T_g - T_C) + \sigma \zeta (T_g^4 - T_C^4) \right] - \left| \Gamma(-\Delta H_{C-steam}) \right|$ $\tag{2.7}$

Gas:

$$\frac{d}{dx}((1-\varepsilon)\rho_g u_g C_{pg} T_g) = -N_C \pi d_p^2 \left[ h_C (T_g - T_C) + \sigma \zeta (T_g^4 - T_C^4) \right] + \frac{\Delta \dot{n}_{co} H_{rxn,water-gas}}{(1-\varepsilon) A_T \Delta x} + \frac{4\dot{q}}{d_T} \tag{2.8}$$

The subscript '$C$' indicates the solid phase, and '$g$' indicates the gas phase. The axial variation of the particle diameter was modeled as:

$$\frac{d(d_p)}{dx} = -\frac{1}{u_C}\frac{2}{\rho_C}\frac{k_s P_t D_{H_2O-mix} MW_C}{\left(\frac{k_s d_p R_u T_g}{2} + D_{H_2O-mix} MW_C\right)} Y_{H_2O} \qquad (2.9)$$

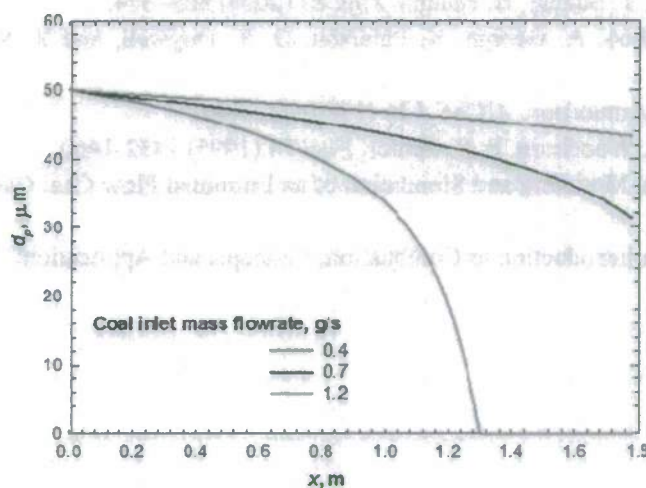Initial results of the unified model are shown in Figures 2.8-2.9.



**Figure 2.8 Axial variation of coal particle diameter for varying inlet mass flow rates of coal.**

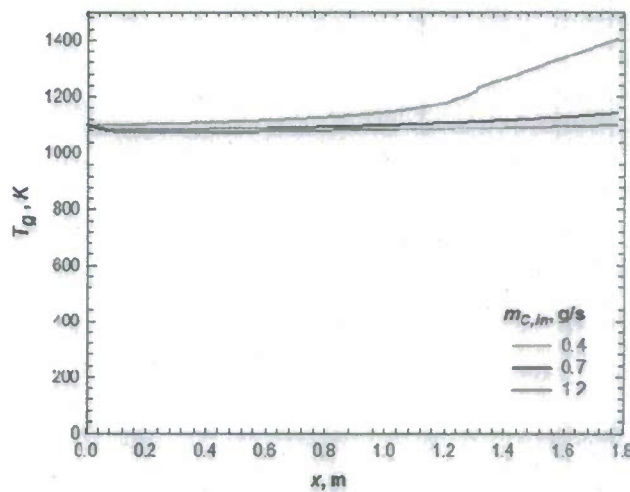$\dot{m}_{g,in} = 1.2$ g/s, $d_{p,in} = 50\mu m$, **and external heating of 12 kW/m$^2$.**



**Figure 2.9: Axial variation of gas phase temperature for varying inlet mass flow rates of coal.**

$\dot{m}_{g,in} = 1.2$ g/s, $d_{p,in} = 50\mu m$, **and external heating of 12 kW/m$^2$.**

## 2.4 References

[2.1] A.J. Minchener, *Fuel* 84 (2005) 2222-2235.

[2.2] K.H. van Heek, H. Juntgen, W. Peters, *Journal of the Institute of Fuel* 46 (1973) 249-258.

[2.3] D.W. Gregg, R.W. Taylor, J.H. Campbell, J.R. Taylor, A. Cotton, *Solar Energy* 25 (1980) 353-364.

[2.4] J.L. Johnson, "Kinetics of coal gasification", John Wiley & Sons, 1979.

[2.5] S. Lin, M. Harada, Y. Suzuki, H. Hatano, *Fuel* 83 (2004) 869–874.

[2.6] A. Cousins, Y. Zhuo, A. George, N. Paterson, D. R. Dugwell, and R. Kandiyoti, *Energy Fuels* 22(2008) 2491-2503.

[2.7] B. Srinivas, N. R. Amundson, *AIChE J* 26 (1980) 487-496.

[2.8] D. Vamvuka, E. T. Woodburn, P. R. Senior, *Fuel* 74 (1995) 1452-1460.

[2.9] R. Govind, J. Shah, Modeling and Simulation of an Entrained Flow Coal Gasifier, AIChE J., 30 (1) (1984) 79-91.

[2.10]   S.R. Turns, "An Introduction to Combustion, Concepts and Applications", McGraw Hill (2000) 524-531.

### 3.0 Flame Structure of Alternative Jet Fuels

### 3.1 Burner Design and Measurements

A new counter-flow burner system was designed and fabricated. Initially, the utilization of our available counter-flow burner systems for both atmospheric pressure and elevated-pressure measurements was planned. In preparation, an extensive series of dual-pump CARS measurements in methane-fueled and hydrogen-fueled counter-flow flames were performed. Comparison of experimental profiles for methane-fueled flames and profiles calculated using OPPDIF were in excellent agreement for some flame conditions and were not in good agreement for other flame conditions, in particular for partially premixed methane-fueled counter-flow flames. For hydrogen-fueled flames, especially with significant dilution, the shapes of the experimental and theoretical profiles were similar, but the spatial locations of the profile peaks were different.

It was concluded that the measurements of the velocity field were needed for rigorous comparison between experimental profiles and calculations of counter-flow flames. In our previous atmospheric-pressure and elevated-pressure flame systems, a porous, sintered metal plug was placed at the exit of the fuel and oxidizer nozzles, precluding the use of particle-scattering-based velocimetry methods; therefore, a new counter-flow burner system featuring contracting nozzle sections for both the fuel and oxidizer streams was designed and fabricated. This system has the great advantage that the flow can be seeded with particles and thus particle-imaging velocimetry (PIV) measurements of the velocity field can be performed. The significant area contraction of the nozzles would ensure uniform flow at the nozzle exit. The PIV measurements would be used to verify the uniformity of the exit profiles. In addition, with a porous metal plug at the exit plane, clogging of the metal plug due to fuel pyrolysis would be a major concern, especially for premixed flames. Clogging due to fuel pyrolysis would not be a concern for the new burner system with contracting nozzles, although flashback may be more of a concern.

The new burner system is shown in Figures 3.1 through 3.3. Figure 3.1 shows a picture of the fully-assembled burner system. The construction details of the nozzles are shown in Figure 3.2, and an exploded view of the nozzles is displayed in Figure 3.3. Each nozzle of the counter-flow burner system was designed with four flow-settling channels so that the total height can be adjusted to achieve a uniform velocity profile at the nozzle exit. The oxidizer and fuel nozzles were fabricated using stainless steel, while the supporting structure was fabricated from aluminum. The top mounting plate, to which the oxidizer nozzle is attached, was fabricated so that the exhaust gases escape with minimal resistance to their flow.

After assembly of the counter-flow burner, the new burner system was tested by stabilizing various laminar, non-premixed $CH_4/O_2/N_2$ flames. Stable flat flames were obtained at global strain rates up to 300 /s. The maximum strain rate corresponds to a total volumetric flow rate of 14.2 slpm for each nozzle while maintaining a separation distance of 10 mm between the two nozzles of the burner. Photographs of the flames at four different strain rates for a mixture of 50% $CH_4$ and 50% $N_2$ in the fuel stream and 21% $O_2$ and 79% $N_2$ in the oxidizer stream are shown in Figure 3.4.

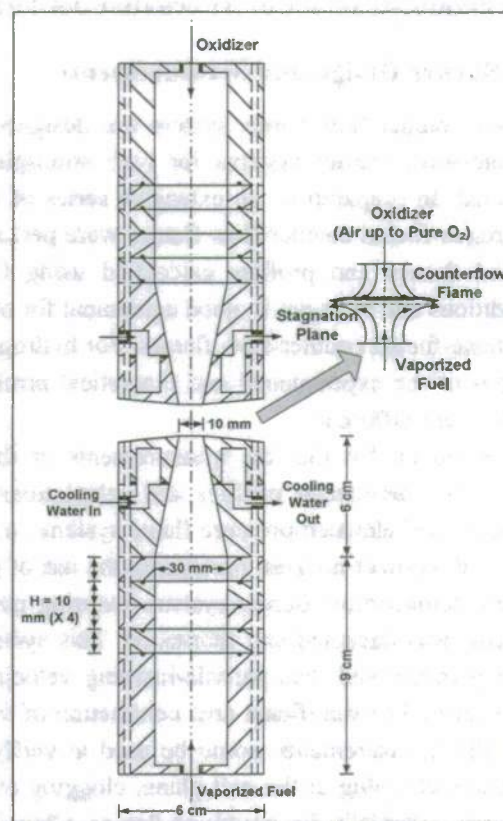**Figure 3.1: Photograph of the new counter flow burner.**



**Figure 3.2: Schematic diagram of the opposed-jet, counter-flow burner system using specially-contoured nozzles.**

Since no porous metal plugs were used at the exit of the contracting nozzles, the reactant flow could be seeded with particles to perform particle imaging velocimetry (PIV) measurements to understand the flow field. These PIV measurements would be performed using a Spectra-Physics Quanta-Ray PIV 400-10 Nd:YAG laser in the near future. The counter-flow burner system was moved from Prof. Lucht's laboratory temporarily to Prof. Gore's laboratory to perform these PIV measurements.
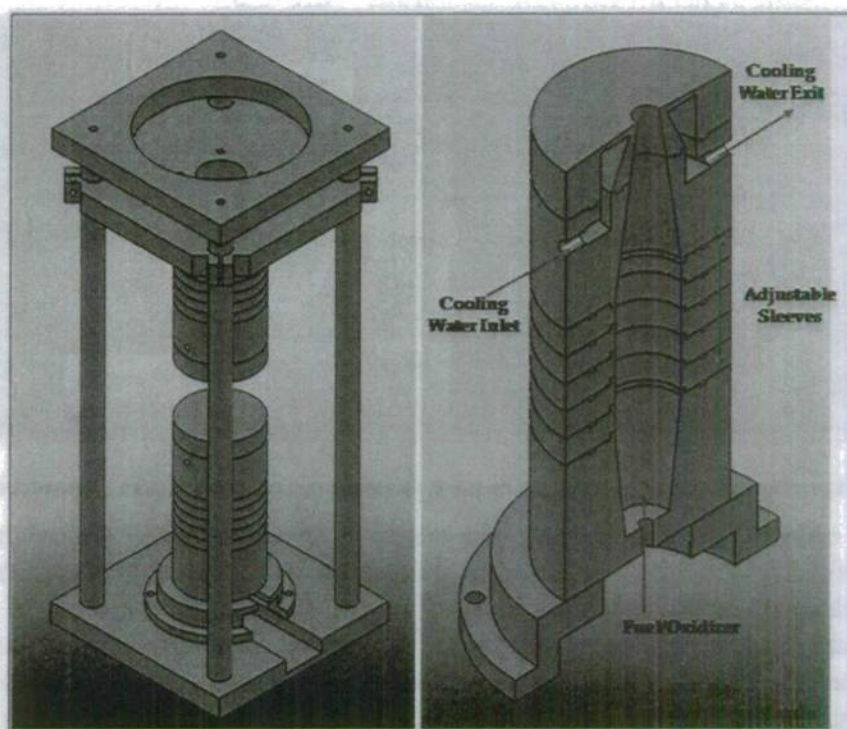
**Figure 3.3: Exploded view showing the construction of the fuel/oxidizer nozzles.**



Strain Rate = 100 s

Strain Rate = 180 s

Strain Rate = 220 s
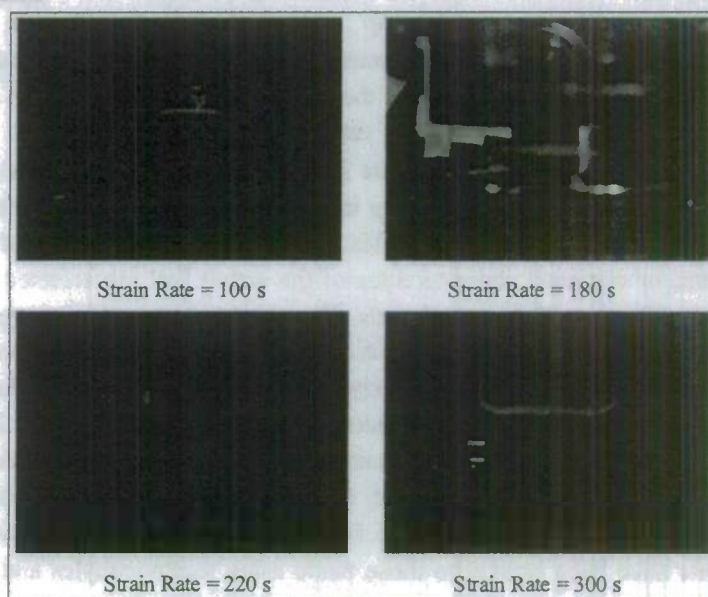
Strain Rate = 300 s

**Figure 3.4: Photographs of non-premixed $CH_4/O_2/N_2$ flames at global strain rates upto 300 s$^{-1}$.**

The burner system mounted near the PIV laser system along with the PIV cameras is shown in Figure 3.5. The equipment to seed particles in the relatively low velocity reactant streams was available in Prof. Gore's laboratory. Such seeding of particles was necessary to measure three velocity components in a 7.1-cm methane pool fire.
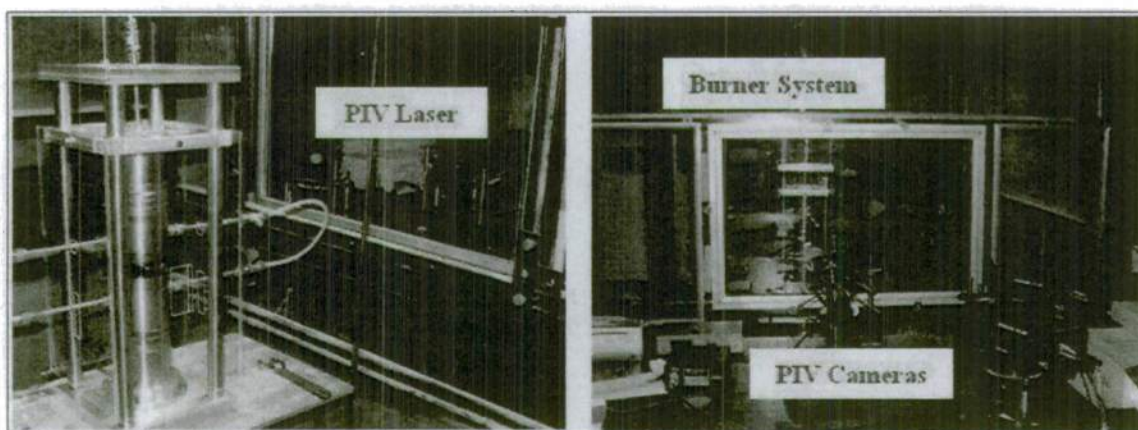
**Figure 3.5: Experimental setup to perform the particle imaging velocimetry (PIV) measurements.**

The study of counter-flow premixed and non-premixed flames has been planned by varying the compositions of fuel (pure n-heptane, n-decane, n-dodecane, as well as mixtures of these fuels to simulate realistic jet fuels) and that of the oxidizer (from air to pure oxygen). The entire burner system will be mounted on motorized translation stages to scan the measurement volume in the axial and radial directions of the flame. High-performance linear translation stages were purchased to translate the new counter-flow burner system in the axial and radial directions. These stages (Newport Corporation ILS-100CC and IMS-100V) are encoded and can be computer-controlled for accurate movement of the entire burner system. This system would be useful for performing two-dimensional (axial and radial) scans across the flames when performing dual-pump coherent anti-Stokes Raman scattering (CARS) measurements to obtain temperature and major species concentration data. Such detailed two-dimensional scans are necessary to investigate whether or not the simplifying one-dimensional assumption typically considered in flame codes such as OPPDIF [3.1] is valid.

The liquid fuel vaporization system shown in Figure 3.6 was designed. Liquid fuels derived from sources such as natural gas, coal, and biomass are becoming increasingly important for civilian and defense usage. Commercially available jet fuels are usually complex. Often surrogate mixtures that adequately represent the desired physical and/or chemical characteristics of the actual fuel are selected to gain fundamental knowledge regarding combustion of the actual fuels. The accuracy of predictions regarding performance of these fuels in gas turbines and propulsion systems obtained from simulations depends on the robustness of the sub-mechanisms for individual fuel components. For gasoline-based fuels, detailed kinetic mechanisms for n-heptane and iso-octane have been developed and validated [3.2, 3.3]. On the other hand, for jet and diesel fuels, the major straight chain paraffin components are n-decane and n-dodecane. The ignition and flammability characteristics of these hydrocarbons are different. Detailed kinetic mechanisms for n-decane and n-dodecane have been developed [3.4-3.8]; however, detailed flame structure measurements have been limited to those made using thermocouples and gas chromatography [3.4, 3.5].
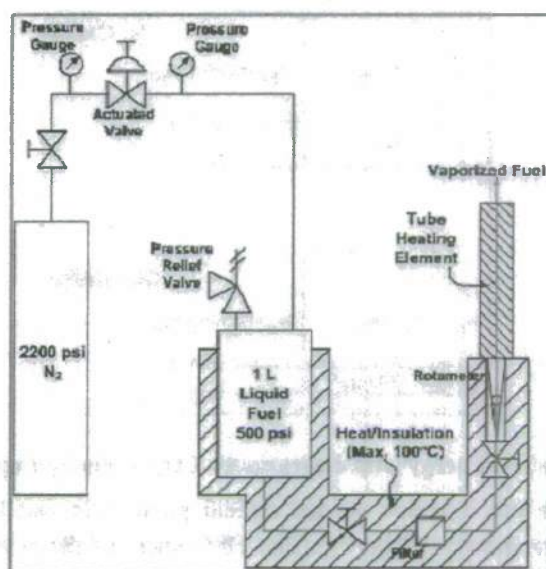
**Figure 3.6: Schematic of the system to vaporize the liquid fuel at desired pressure.**

The availability of benchmark experimental data for the individual components of jet fuels would be extremely valuable to validate detailed flame structure. The primary goal of this work would be to provide such experimental data for flames burning fuels such as n-heptane, n-decane, n-dodecane, and JP-10 ($C_{10}H_{16}$) using advanced laser diagnostic techniques. Measurements of temperature and major species concentration shall be conducted in stable, well-characterized laminar counter-flow flames at atmospheric pressure initially and then at higher pressures.

Dual-pump coherent anti-Stokes Raman scattering (CARS) temperature and major species concentration measurements have been planned. In dual-pump CARS [3.9], two narrowband pump lasers would be used in conjunction with a single broadband Stokes laser to monitor two species via two separate, three-color wave mixing processes. Accurate temperature measurements are critical to test kinetic models of flames burning the selected individual components that constitute jet fuels. We shall employ dual-pump, broadband $H_2/N_2$, $O_2/N_2$ and $CO_2/N_2$ CARS in our target flames. In this manner, we shall have three independent temperature measurements (using three different pairs of molecules), as well as quantitative measurements of four major species: $H_2$, $O_2$, $CO_2$, and $N_2$. These temperature and major species concentration profiles will provide a rigorous test for chemical kinetic mechanisms and transport models.

An energy level diagram for the simultaneous measurement of $N_2$ and $CO_2$ CARS spectra is shown in Figure 3.7, and the proposed experimental system is shown in Fig. 3.8. For the $CO_2$ molecule, the Raman transitions near 1300 cm$^{-1}$ are excited by the 560-nm pump and 607-nm Stokes beams, and the 532-nm probe beam is scattered from the induced polarization to generate the CARS (or anti-Stokes) signal at 496 nm. For the $N_2$ molecule, the 532-nm and 560-nm beams are reversed; the 2330 cm$^{-1}$ Raman transitions are excited by the 532-nm pump and 607-nm Stokes beams, and the 560-nm probe beam is scattered from the induced polarization to generate the CARS (or anti-Stokes) signal at 496 nm. The $N_2$ and $CO_2$ signals are generated at the same wavelength and can be detected using a single CCD camera. We have performed several experiments over the last few years with dual-pump $H_2/CO_2$ and $N_2/CO_2$ systems, including a detailed study of the exhaust stream of a swirl-stabilized combustor fueled with JP-8 [3.10-3.13].
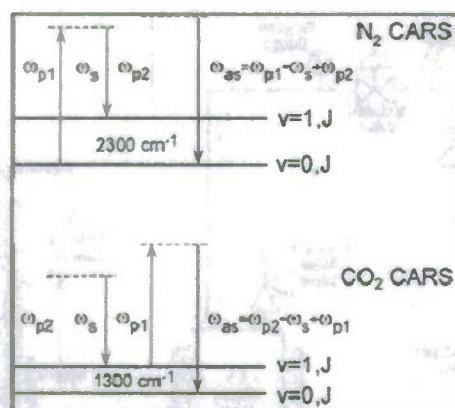
**Figure 3.7: Energy level diagrams for $CO_2/N_2$ dual-pump CARS.**

The system architecture for the injection seeded optical parametric oscillator (OPO) and pulsed dye amplifier (PDA) systems are shown in Fig. 3.9. The OPO stage of the system consists of two counter-rotating beta barium borate ($\beta$-BBO) crystals. These crystals are pumped with the 355-nm single-longitudinal-mode (SLM) third-harmonic output of an injection-seeded Nd:YAG laser. The OPO stage would be seeded with a distributed feedback (DFB) diode laser or with an external cavity diode laser (ECDL) at 970 nm. The result of the optical parametric process in the $\beta$-BBO crystal is the amplification of the input seed beam at the idler wavelength of 970 nm and the generation of an SLM signal beam at 560 nm. The signal beam output from the OPO stage would then be amplified in a single PDA. The PDA would be pumped by the second-harmonic 532-nm beam from the injection-seeded Nd:YAG laser.
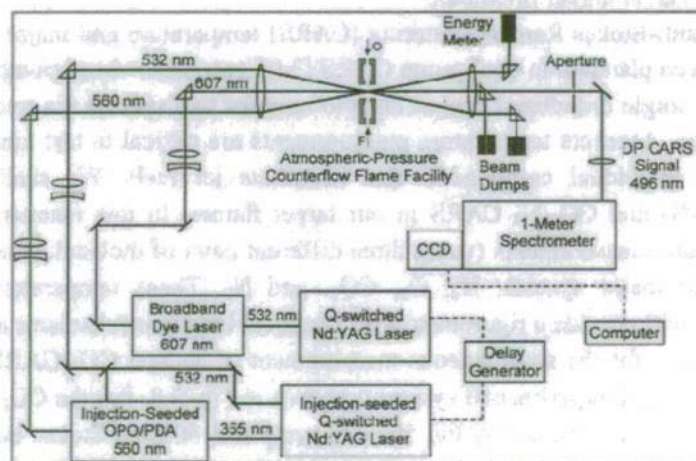


**Figure 3.8: Experimental diagram for the dual-pump CARS system for simultaneous measurement of temperature, $N_2$, and $CO_2$.**
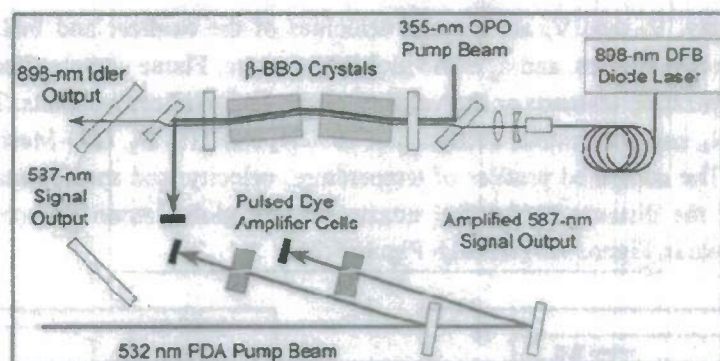
**Figure 3.9: Injection-seeded OPO/PDA system for the generation of SLM pump radiation used in dual-pump CARS experiment.**

The SLM character of the 560-nm beam minimizes shot-to-shot fluctuations in the laser spectrum, thereby decreasing shot-to-shot fluctuations in the fitted temperature and species concentrations. Instrumental fluctuations are decreased by almost a factor of two based on observation of the behavior of the signal when the 532-nm beam from Nd:YAG laser was single-mode versus multi-mode.

## 3.2 Computational Studies of Flame Structure of Alternative Jet Fuels

In parallel with the experimental work, we have conducted modeling studies of premixed and nonpremixed flames for major surrogate jet fuel species, including n-heptane, n-decane, and n-dodecane. The focus has been on understanding the detailed kinetic mechanisms, thermodynamic properties, and transport properties of these species. Meanwhile, we have been using the PREMIX [3.1] and OPPDIF [3.14] modules of CHEMIKIN [3.15] to simulate premixed and non-premixed flames of simple gaseous fuels. Through these studies we have obtained adequate understanding of existing kinetic models for surrogate jet fuels, as well as their potential performance. We have become familiar with CHEMKIN subroutines, which would assist us to implement new complex kinetics of heavy liquid fuels and radiation models in the near future. Our preliminary computational results, as well as the experimental and computational data in literature, have indicated that large discrepancies exist in the predicted flame speed and flame structure using several different reaction mechanisms. Discrepancies were also found between predicted and measured flame speeds. Presence of these discrepancies indicated that flame speed comparison is not sufficient for evaluating current kinetic mechanisms. It is necessary to obtain accurate and detailed profiles of flame structure, such as temperature and species concentrations, as proposed by this study.

Our modeling focused on the non-premixed counterflow $CH_4/O_2/N_2$ flames. The flame conditions were the same as the experiments, which are described in Task 3, Flame Structure of Alternative Jet Fuels. The purpose of studying gaseous fuel initially was to test the burner system and to validate the velocity measurements using PIV and the temperature measurements using CARS thermometry. Three different global strain rates (20 /s, 40 /s, and 60 /s) were considered, and the separation distance between the fuel and oxidizer nozzles was maintained at 2 cm. The corresponding flow velocities at the nozzle exit are 10, 20, 30 cm/s, respectively, for the 3 strain rates and the given nozzle distance.

$$a_g = 2\frac{|V_0|}{L}\left(1+\frac{|V_r|}{|V_0|}\sqrt{\frac{\rho_r}{\rho_0}}\right) \qquad (3.1)$$

where, $\rho$ is the density, $V_O$ and $V_F$ are the gas velocities of the oxidizer and fuel, $L$ is the separation distance between the two nozzles, and $a_g$ is the global strain rate. Flame stretch effects can be studied by varying either the separation distance or the velocity of the fuel/oxidizer reactants. The fuel consisted of 25% $CH_4$ and 75% $N_2$, and the oxidizer consisted of 79% $N_2$ and 21% $O_2$. GRI-Mech 3.0 [3.16] was used for the simulations. The computed profiles of temperature, velocity, and species concentration along the axis as functions of the distance to the fuel nozzle exit for global strain rates of 20, 40, and 60 /s, respectively, are shown in Figure 3.10 through Figure 3.21.
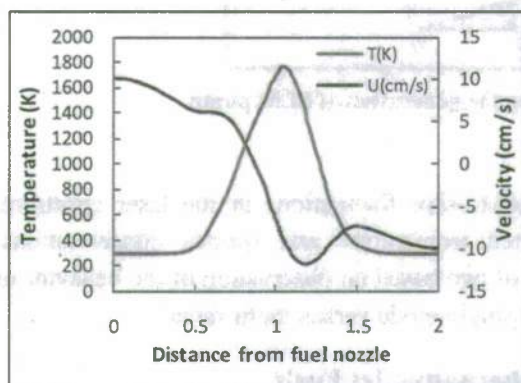


Figure 3.10: Computed profiles of temperature and velocity along the axis as a function of the distance from fuel nozzle. The global strain rate is 20 s$^{-1}$.
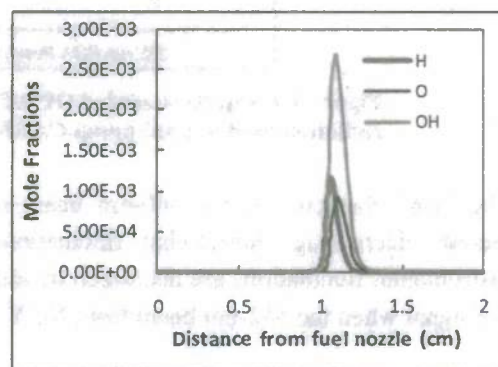


Figure 3.11: Computed profiles of H, O, and OH concentrations along the axis as a function of the distance from fuel nozzle. The global strain rate is 20 s$^{-1}$.
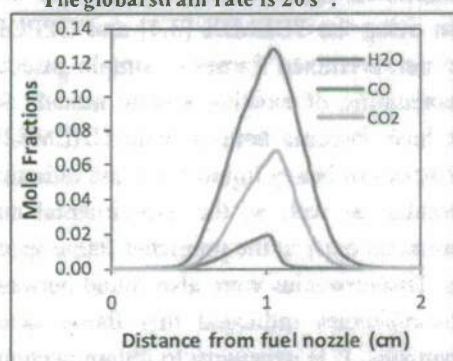


Figure 3.12: Computed profiles of $H_2O$, CO, and $CO_2$ concentrations along the axis as a function of the distance from fuel nozzle. The global strain rate is 20 s$^{-1}$.
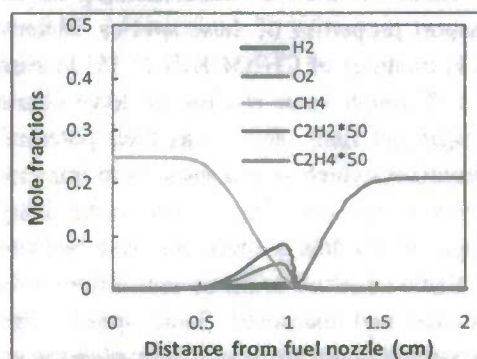


Figure 3.13: Computed profiles of $H_2$, $O_2$, $CH_4$, $C_2H_2$ and $C_2H_4$ concentrations along the axis as a function of the distance from fuel nozzle. The global strain rate is 20 s$^{-1}$.
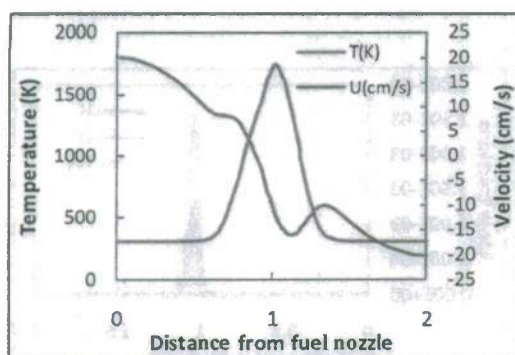
Figure 3.14: Computed profiles of temperature and velocity along the axis as a function of the distance from fuel nozzle. The global strain rate is 40 s⁻¹.
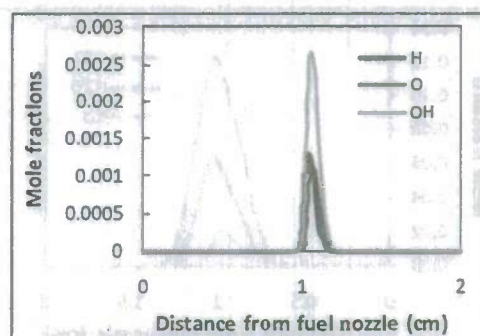


Figure 3.15: Computed profiles of H, O, and OH concentrations along the axis as a function of the distance from fuel nozzle. The global strain rate is 40 s⁻¹.
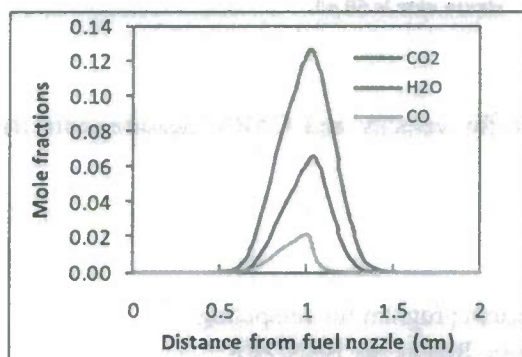


Figure 3.16: Computed profiles of $H_2O$, CO, and $CO_2$ concentrations along the axis as a function of the distance from fuel nozzle. The global strain rate is 40 s⁻¹.



Figure 3.17: Computed profiles of $H_2$, $O_2$, $CH_4$, $C_2H_2$ and $C_2H_4$ concentrations along the axis as a function of the distance from fuel nozzle. The global strain rate is 40 s⁻¹.



Figure 3.18: Computed profiles of temperature and velocity along the axis as a function of the distance from fuel nozzle. The global strain rate is 60 s⁻¹.



Figure 3.19: Computed profiles of $H_2$, $O_2$, $CH_4$, $C_2H_2$ and $C_2H_4$ concentrations along the axis as a function of the distance from fuel nozzle. The global strain rate is 60 s⁻¹.

Figure 3.20: Computed profiles of $H_2O$, CO, and $CO_2$ concentrations along the axis as a function of the distance from fuel nozzle. The global strain rate is 60 $s^{-1}$.
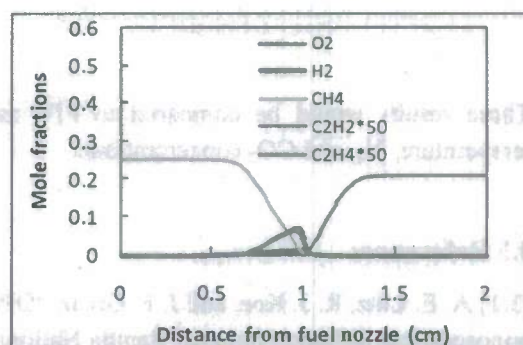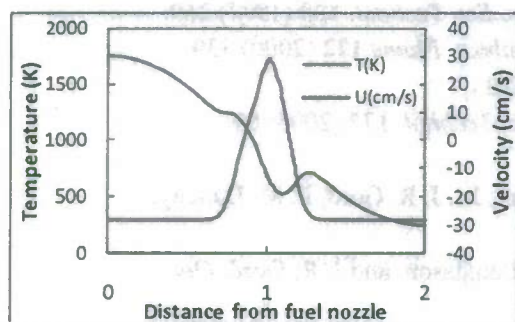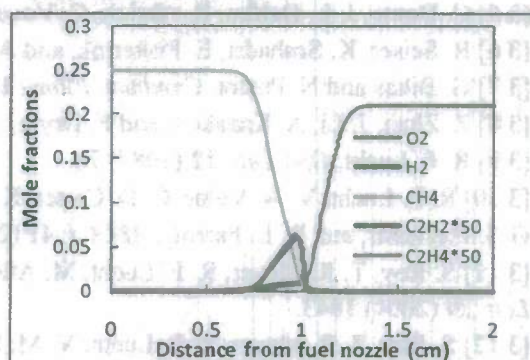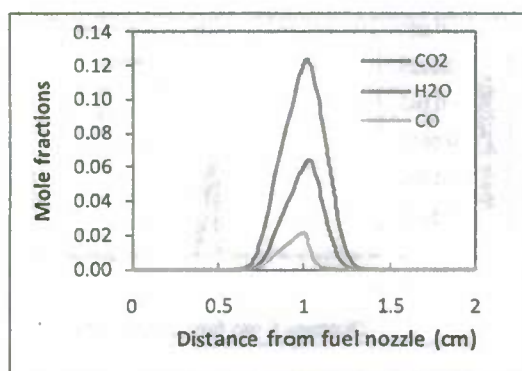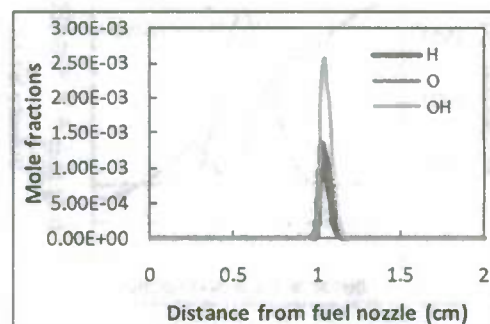


Figure 3.21: Computed profiles of H, O, and OH concentrations along the axis as a function of the distance from fuel nozzle. The global strain rate is 60 $s^{-1}$.

These results would be compared to PIV measurements for velocity and CARS measurements for temperature, $N_2$, and $CO_2$ concentrations.

## 3.3 References

[3.1] A. E. Lutz, R. J. Kee, and J. F. Grcar, "OPPDIF: A Fortran program for computing opposed-flow diffusion flames," Sandia National Laboratories, Report No. SAND96-8243 (1996).

[3.2] H. J. Curran, P. Gaffuri, W. J. Pitz, C. K. Westbrook, *Combust. Flame* **114** (1998) 149.

[3.3] H. J. Curran, P. Gaffuri, W. J. Pitz, C. K. Westbrook, *Combust. Flame* **129** (2002) 253.

[3.4] C. Doute, J. L. Delfau, R. Akrich, C. Vovelle, *Combust. Sci. Technol.* **106** (1995) 327.

[3.5] C. Doute, J. L. Delfau, R. Akrich, C. Vovelle, *Combust. Sci. Technol.* **130** (1997) 269.

[3.6] R. Seiser, K. Seshadri, E. Piskernik, and A. Linan, *Combust. Flame* **122** (2000) 339.

[3.7] G. Bikas and N. Peters, *Combust. Flame* **126**, 1456 (2001).

[3.8] Z. Zhao, J. Li, A. Kazakov, and F. Dryer, *Combust. Sci. Technol.* **177** (2005) 89.

[3.9] R. P. Lucht, *Opt. Lett.* **12** (1987) 78.

[3.10] R. P. Lucht, V. N. Velur, C. D. Carter, K. D. Grinstead, Jr., J. R. Gord, P. M. Danehy, G. J. Fiechtner, and R. L. Farrow, *AIAA J.* **41** (2003) 679.

[3.11] S. Roy, T. R. Meyer, R. P. Lucht, M. Afzelius, P. E. Bengtsson, and J. R. Gord, *Opt. Lett.* **29** (2004) 1843.

[3.12] S. Roy, T. R. Meyer, R. P. Lucht, V. M. Belovich, E. Corporan, and J. R. Gord, *Combust. Flame* **138** (2004) 273.

[3.13] T. R. Meyer, S. Roy, R. P. Lucht, and J. R. Gord, *Combust. Flame* **142** (2005) 52.

[3.14] R. J. Kee, F. M. Rupley and J. A. Miller, Chemkin-II: A FORTRAN Chemical Kinetics Package for the Analysis of Gas-Phase Chemical Kinetics, *Sandia National Laboratories,* (1989)

[3.15] Puri, I. K., and Seshadri, K., *Combust. Flame* 65 (1986) 137–150.

[3.16] http://www.me.berkeley.edu/gri_mech/version30/text30.html

## 4.0 Conclusions

The first year of the project involved design calculations and construction of apparatuses for biomass fast hydropyrolysis, hydrodeoxygenation, and gasification considered critical for the newly emerging synthetic fuel economy. Control of $CO_2$ emissions from these processes, as well as obtaining the highest overall energy and carbon conversion efficiencies, have been related opportunities. The specific conclusions from the present project are listed as:

(1) System level and limited detailed chemistry calculations have shown that significant reductions in net $CO_2$ emissions are possible using the excess hydrogen gasification, fast hydropyrolysis, and hydrodeoxygenation processes. As an example, the excess hydrogen gasification process showed reductions of up to 50% in $CO_2$ emissions.

(2) Processes involving biomass handling, transport, delivery, flow, and control have been difficult to manage because of raw material variability, particle softening, melting, and agglomeration, as well as wall fouling and tube clogging due to char formation.

(3) Control of char formation was shown to be possible using optimum heating rates, and design of biomass reactors using this principle has been initiated.

(4) An optically accessible coal gasifier that utilizes hydrogen-oxygen flame generated steam and excess hydrogen for $CO_2$ control has been built.

(5) System level calculations for the gasifier have shown feasibility of near-complete gasification of particles with diameters on the order of 50 microns.

(6) External energy input, methane formation, and char and ash formation have been managed as significant issues in the present gasifier design.

(7) Design of an opposed flow burner with well defined initial and boundary conditions was necessary for experiments with alternate fuels, including biofuels. These issues are well recognized and being addressed by many investigators in the AFOSR propulsion program.

(8) Application of detailed chemistry modeling and laser diagnostics to the fuel synthesis economy was confirmed as the new opportunity and will be pursued in years 2 and 3 of the current program.

## 5.0 Participating Personnel

This project represents a multidisciplinary collaboration between Chemical Engineers, Mechanical Engineers, and Aerospace Engineers benefitting from the knowledge base of all three disciplines. All personnel listed below are accessible to help on all parts of the project in addition to being focused on the three tasks as listed in the following.

### Biomass Fast Hydropyrolysis: School of Chemical Engineering

1. Rakesh Agrawal, Professor, PI. Oversaw and participated in all aspects of the research related to biomass hydropyrolysis. Provides the overall vision for a sustainable transportation fuel economy.

2. Fabio H. Ribeiro, Professor, participating investigator. Participated in design and oversaw construction and operation of all equipment, participated in design and interpretation of all experiments.

3. W. Nicholas Delgass, Professor, participating investigator. Participated in design of equipment and design and interpretation of all experiments.

4. Jun Wang, Post-Doctoral Research Associate. Built and operated continuous low pressure pyrolysis unit used for visualization studies.

5. Andrew Smeltz, Post-Doctoral Research Associate, project manager. Oversaw and helped design and build all experimental apparatuses, responsible for compiling research reports from group members.

6. Fernando Resende, Post-Doctoral Research Associate. Helped design and operate continuous low pressure pyrolysis unit used for visualization studies.

7. Piotr Gawecki, Graduate Student. Designed, built, and operated micro batch pyrolysis reactor used for visualization studies.

8. Dharik Mallapraganda, Graduate Student. Performed overall process calculations to support the experimental studies.

9. Navneet Singh, Graduate Student. Performed overall process calculations which established the research direction and led to motivation for the experimental studies.

10. Yury Zvinevich, Director of the Advanced Spectroscopic Facility. Helped design and build experimental apparatuses used in the study.

### Optically Accessible Gasifier and Flame Structure Studies: School of Mechanical Engineering and School of Aeronautical and Astronautical Engineering

1. Jay Gore, Professor, Co-PI. Oversaw and participated in all aspects of the research related to the optically accessible gasifier and flame structure studies. Provided overall coordination and support across the project.

2. Robert Lucht, Professor, participating investigator. Oversaw the design, construction and operation of counter flow burner experiment for flame structure studies. Provided expertise in design of experiment for optical diagnostics of gasifier.

3. Li Qiao, Assistant Professor, participating investigator, Oversaw the computational work related to flame structure studies. Provided her expertise related to coal gasifier modeling.

4. Scott Meyer, Operational director Maurice J. Zucrow Labs, Oversaw the design and construction of gasifier experimental apparatus and laboratory infrastructure.

5. Sameer V. Naik, Visiting Assistant Professor, Participated in design and operation of experiment for flame structure studies. Provided his expertise in design of experiment for optical diagnostics of gasifier.

6. Anup Sane, Graduate Student, Performed overall process calculations which established the research direction, led the design process of the high pressure particle feeder and optical diagnostics system, responsible for compiling research reports from group members.

7. David Blunck, Graduate Student, Oversaw and participated in the design process of gasifier rig, Worked as a project coordinator.

8. Rohan Gejji, Graduate Student, Led the design and manufacture of chemical steam generator and the assembly process of the optically accessible gasifier arrangement for gasifier.

9. Indraneel Sircar, Graduate Student, Led the design of the reactor vessel, support structure, and control and diagnostics system for the gasifier arrangement.

10. Aman Satija, Graduate Student, Performed experimental work for flame structure studies.

11. Deepti Singh, Graduate Student, Premixed flame speed measurements and computations for alternate fuels.

12. Devashish Bangar, Undergraduate Student. Learned laboratory practices.


## 6.0 Publications and Presentations

### 6.1 Publications

1. Singh, N. R., Delgass, W. N., Ribeiro, F. H., and Agrawal, R., "Estimation of Liquid Fuel Yields from Biomass", Environmental Science and Technology 44 2010 p5298-5305

2. Agrawal, R., and Singh, N. R., "Solar Energy to Biofuels", Review of Chemical and Biomolecular Engineering 1 2010 p343-364

3. Anup Sane, Yuan Zheng, and Jay Gore, "A Study of Steam gasification of Coal with $CO_2$ Control using $H_2$," 6th US National Combustion Meeting, May 17-20, 2009, Ann Arbor, MI.

4. Indraneel Sircar, Rohan Gejji, Anup Sane, David Blunck, Scott Mayer and Jay Gore, "Design and Testing of a High Pressure and Temperature, Optically Accessible, Entrained Flow Coal Gasifier", ASME/JSME 8th Thermal Engineering Joint Conference, Abstract accepted, Paper in preparation.

5. Indraneel Sircar, Rohan Gejji, Anup Sane, David Blunck, Scott Mayer and Jay Gore, "Design and Construction of an Optically-Accessible Coal Gasifier for $CO_2$ Reduction using Excess $H_2$", AIAA ASM Conference 2011, Paper in review.

## 6.2 Presentations

1. Rakesh Agrawal, "Energy Solutions for a Fossil Fuel Deprived Future", Andlinger Energy Lecture, Princeton University, Princeton, February, 2009.
2. Rakesh Agrawal, "Transportation Fuel in a Fossil Fuel Free world", Renewable Energy World 2009, Las Vegas, March 2009.
3. Rakesh Agrawal, "Sustainable Energy Utilization and Transformation", George W. Woodruff School of Mechanical Engineering's Sustainable Energy Pathways and Solutions Workshop, Georgia Tech., Atlanta, April 2009.
4. Rakesh Agrawal, "Synergistic Processes for Biofuels", Purdue Biofuels Symposium, West Lafayette, In, May 2009.
5. Rakesh Agrawal, "Transportation Fuel in a Solar Economy", Keynote Lecture, FOCAPD, Breckenridge, Co, June 2009.
6. Rakesh Agrawal, "Synergistic Processes for Biofuels", Plenary Lunch Lecture, BioFuels Conference-The Next Generation of Biofuels, Mississippi State University, Jackson, Ms, August 2009
7. Rakesh Agrawal, "Energy Solutions for a Fossil Fuel Deprived Future", Pioneers in Energy Lecture, Purdue University, West Lafayette, IN, September 2009.
8. Rakesh Agrawal, "More Liquid Fuel from Biomass", Indo-US Workshop on Climate and Energy Futures, Chennai, India, October 2009.
9. Rakesh Agrawal, "Transportation Fuel Solutions Using Renewable Energy", RTI Fellows Symposium, RTI International, Research Triangle Park, NC, November 2009.
10. Rakesh Agrawal, *"Solar Based Sustainable Energy Solutions",* Maddox Solar Energy Series, Whitacre College of Engineering at Texas Tech University, February, 2010.
11. Rakesh Agrawal, "Role of Biomass to Liquid Fuel in a Solar Economy", C3Bio Meeting. Purdue University, May, 2010.
12. Rakesh Agrawal, "Solar Based Sustainable Energy Solutions", Plenary Lecture, 2nd International Symposium on Sustainable Chemical Product and Process Design (ISSCPPE), Hangzhou, China, May, 2010.